International Journal of Hydrogen Energy 238 (2026) 155383

Contents lists available at ScienceDirect

International Journal of Hydrogen Energy

journal homepage: www.elsevier.com/locate/he

Optimized NiFe-LDH catalyst layers boost anion exchange membrane water electrolyzer performance and durability

Irina Galkina [a,*], Alaa Y. Faid [b], Nikita Grigorev [c], Wulyu Jiang [a], Patrick Borowski [d], Svein Sunde [b], Meital Shviro [a,e], Werner Lehnert [a,f], Fabian Scheepers [a], Anna K. Mechler [a,g,h]

[a] Forschungszentrum Jülich GmbH, Institute of Energy Technologies, Electrochemical Process Engineering (IET-4), 52425, Jülich, Germany
[b] Department of Materials Science and Engineering, Norwegian University of Science and Technology, 7034, Trondheim, Norway
[c] Institute of Mineral Engineering (GHI), RWTH Aachen University, 52056, Aachen, Germany
[d] Evonik Operations GmbH, 45772, Marl, Germany
[e] Chemistry and Nanoscience Center, National Renewable Energy Laboratory (NREL), Golden, 80401, Colorado, United States
[f] RWTH Aachen University, Faculty of Mechanical Engineering, Modelling in Electrochemical Process Engineering, 52056, Aachen, Germany
[g] RWTH Aachen University, Electrochemical Reaction Engineering (AVT.ERT), 52056, Aachen, Germany
[h] JARA-ENERGY, 52056, Aachen, Germany

ARTICLE INFO

Keywords:
Anion exchange membrane water electrolysis
Catalyst milling
Electrode optimization
NiFe-LDH
Catalyst layer
Catalyst dispersion

ABSTRACT

The optimization of anion exchange membrane water electrolyzers (AEMWEs) relies on active, stable catalysts and well-designed catalyst layers. This study investigates the impact of tumbler ball milling on a nickel–iron layered double hydroxide (Ni_3Fe-LDH) catalyst for the oxygen evolution reaction (OER). Milling reduced catalyst clusters from 1-100 μm to 30 nm, increasing the geometrical surface area by 8.8-fold. Optimized solvent compositions and dispersing times enhanced catalyst dispersion stability. Tailoring the electrode structure reduced internal electronic resistances and charge-transfer resistances of the membrane electrode assembly. The optimized electrode exhibited outstanding single-cell performance, reaching 1.83 V at 2 A cm^{-2} with stable durability of 1000 h and a minor degradation rate of 62 μV h^{-1}. This work presents a scalable approach to NiFe-LDH catalyst treatment and dispersion control, demonstrating the importance of research and optimization across scales to improve performance and support the practical advancement of hydrogen technologies.

1. Introduction

Facing a significant rise in energy demand and serious environmental challenges, including climate change, renewable power production has attracted great interest over the past few decades. The decreasing costs and rapid optimization of materials and components make renewable energy an increasingly feasible solution [1–3]. One promising method for energy conversion and storage is water electrolysis, which allows the storage of intermittent solar and wind energy as a chemical fuel, namely hydrogen. The anion exchange membrane (AEM) water electrolyzer (WE) is a next-generation electrolyzer technology. It aims to address the shortcomings of both proton exchange membrane (PEM) WE and alkaline WE by integrating the advantages of each and already shows promising results in terms of performance and longevity [4]. The oxygen evolution reaction (OER) is a bottleneck in water electrolysis, presenting sluggish reaction kinetics and complex, four-electron transfer steps [5,6]. The development of abundant, low-cost and efficient catalysts is one of the central aims of current research in renewable energy.

Transition metal (Ni, Fe, Co) oxides and their derivatives are promising candidate catalyst for AEMWE due to their affordability and excellent OER performance [1,7,8]. In particular, layered double hydroxides (LDHs) have drawn significant interest due to the simple synthesis, as well as the cost-effectiveness and high catalytic activity with respect to OER. The intrinsic layered structure of LDH materials offers an advantage over bulk oxide mediums, facilitating the efficient diffusion of reaction intermediates and the desorption of gaseous products

* Corresponding author. Forschungszentrum Jülich, Wilhem-Johnen-Straße, 52428, Jülich, Germany.
E-mail addresses: ir.galkina@fz-juelich.de (I. Galkina), alaa.yahia.faid@gmail.com (A.Y. Faid), nikita.grigorev@ilt.fraunhofer.de (N. Grigorev), wulyu.jiang@icfo.eu (W. Jiang), patrick.borowski@evonik.com (P. Borowski), sveinsu@ntnu.no (S. Sunde), meital.shviro@nrel.gov (M. Shviro), werner.lehnert@rwth-aachen.de (W. Lehnert), f.scheepers@fz-juelich.de (F. Scheepers), a.mechler@fz-juelich.de (A.K. Mechler).

https://doi.org/10.1016/j.ijhydene.2026.155383
Received 7 February 2025; Received in revised form 14 April 2026; Accepted 2 May 2026
Available online 4 May 2026

[9–12].

The adjustment of Ni–Fe-LDH design and modifications [13–16], including fine-tuning of the synthesis [9,17–19], catalyst treatment, and element doping [20,21], as well as the resulting catalyst compositions and structural adjustments [22], have yielded significant improvements in intrinsic catalytic activity and catalyst utilization. The latter is defined not only by the actual catalytic activity and stability but also the accessibility of the active sites, described by the electrochemically active surface area (ECSA). For the Ni–Fe-LDH catalysts in particular, the increase in ECSA can be further achieved by the exfoliating process of nanosheets from the LDH bulk or the decrease in nanosheet size as reported previously in the literature [9,19,23,24]. The resulting increased ECSA and catalytic activity is consequently attributed to enhanced anion exchange capabilities between the LDH layers and higher electrochemical accessibility of the inner layer surfaces. Mostly, these insights are derived from electrochemical activity measured in three electrode configurations, which can overlook the more complex interfacial environment present in membrane electrode assemblies (MEAs). Consequently, translating catalyst performance from model systems to practical electrodes, via catalyst ink formulation and electrode fabrication, often remains nontrivial and may suffer from poor catalyst utilization, limited control over catalyst layer (CL) morphology and homogeneity, and mass transport limitations [25,26].

In line with recent AEMWE literature, catalyst optimization at the device level therefore requires addressing not only intrinsic kinetics but also CL utilization and losses associated with electronic and ionic transport networks and morphological non-uniformity within the CL [27]. Moreover, systematic MEA and CL studies have been explicitly identified as scarce, despite their strong influence on catalyst utilization and durability [27,28].

When aiming to enhance catalytic activity and utilization within the entire electrode, the focus should not only be on the comprehensive catalyst treatment but additionally on morphological and structural modifications to the electrode and CL, with the purpose of increasing the number of accessible active sites. Although many studies prioritize the preparation and optimization of catalyst powders and their characterization, the strategy of CL development and optimization has often been underrated. Electrode morphology can impact both the overpotential and ion transport resistance. First, it is influenced not only by the intrinsic catalyst activity but also the effective surface area of the electrode, which is typically tailored in the final steps of catalyst powder treatment and CL formation. From this point of view, there remains a noticeable gap in systematic approaches that correlate catalyst dispersion, layer characteristics and single-cell performance. In particular the effects of processing techniques, such as catalyst tumbler milling and dispersion control, on CL morphology and single-cell performance. Specifically, research on NiFe-LDH-based catalyst inks are rare still essential for achieving optimized catalyst utilization. The control of catalyst dispersions and the formulations themselves should be carefully selected and examined [29]. This is to ensure a high level of catalyst-binder distribution and to yield enhanced triple-phase boundaries (TPB) where the actual electrochemical reaction takes place [30]. Importantly, the dispersion and aggregation state and resulting particle or cluster size distribution in catalyst inks can govern CL microstructure, homogeneity, and electrochemically accessible active sites; however, the processing–structure–performance relationships for dispersion control in electrolyzer catalyst layers remain insufficiently understood, particularly for LDH-based AEMWE electrodes [31–33].

As size reduction strategies can themselves modify catalysts intrinsically, it is also critical to distinguish between (i) intended dispersion or CL engineering and (ii) unintended (or purposely induced) physicochemical changes caused by high-energy milling. For example, ball milling has been used to introduce tensile strain in NiFe hydroxides, modify adsorption of oxygenated intermediates, and enhance OER activity [20]; similarly, ball milling can generate amorphous surface layers in perovskites or alter crystallinity and valence states, which are changes that may improve or degrade OER depending on material and conditions [34–36]. Accordingly, when the goal is to improve electrode fabrication and catalyst utilization without confounding intrinsic catalyst chemistry, lower-energy approaches that primarily reduce agglomeration and improve ink stability are advantageous [35,37]. This motivates the selection of low-energy tumbler milling in the present work, together with comprehensive structural and chemical characterization to verify whether intrinsic catalyst changes occurred.

In this work, we address the aforementioned research gaps by conducting an investigation of catalyst powder treatment, ink formulation and dispersing strategies for the Ni_3Fe-LDH OER catalyst. We employ scalable tumbler ball milling and systematically tune dispersion preparation, while linking the milling effect and ink parameters, specifically the ink composition and dispersing time, to the catalyst layer microstructure, and, subsequently, the single-cell activity and durability. The study presents a straightforward and scalable approach to improving the performance of Ni_3Fe-LDH-based single-cells. The proposed strategy includes simple yet effective catalyst milling and dispersion adjustments steps, paving the way for large-scale applications of the non-platinum group metal (PGM) catalyst Ni_3Fe-LDH.

2. Experimental

2.1. Chemicals and materials

The anode catalyst Ni_3Fe-LDH was synthesized by the co-precipitation method based on the low solubility product of metal ions (Ni^{2+} and Fe^{3+}) in an alkaline solution, as described elsewhere [9]. Commercial platinum on carbon (Pt/C, 60% on high surface area carbon, Alfa Aesar) was used as the cathode catalyst. All aqueous solutions were prepared using Milli-Q water (18.2 MΩ, EMD Millipore). The AEM DURAION® and its corresponding preliminary anion-conducting binder were supplied by Evonik. A nickel fiber substrate (Ni 2GDL30-0.50, 500 μm thick, Bekaert) was used as the porous transport layer (PTL) for the anode side and carbon fiber composite paper (TGP-H-120, 370 μm thick, Toray) was used as the cathode PTL. For KOH, the electrolyte preparation's solid pellets were used (EMSURE®, 85% purity KOH, VWR).

2.2. Milling procedure

The catalyst powder was wet-milled using the tumbler mixer Turbula® T2F (WAB) (Fig. 1). Pure ethanol (EtOH) was employed as the grinding media. A 250 ml PE bottle was filled to the 75 mL mark with Zirconia grinding balls (type ZY-S, >99.79%, SiLibeads) with a diameter of 1.3 mm. The grinding ball size was selected based on the common rule that milling media should be at least twice the characteristic size of the bulk feed material to enable efficient milling [38]. The weight ratio of catalyst-to-grinding balls chosen was 1:25. The slurry was filled to approximately 170 mL of the bottle's volume. The milling was performed at 67 rpm without any stops in between for a duration of 15 h, which was determined to be optimal for achieving a unimodal size distribution of the catalyst particles. 67 rpm correspond to 66 percent of the maximum machine speed. This setting falls within the optimum rotational speed range where the milling media repeatedly lifts and cascades, ensuring effective yet gentle grinding while avoiding centrifuging or media pinning to the vessel wall [39]. During preliminary tests, the slurry temperature was monitored using a thermostat. The maximum recorded temperature was 28 °C, confirming that no heating occurred during the chosen milling time and rotation speed.

2.3. Catalyst ink preparation

For the ink formulation with Pt/C, catalyst powder (500 mg), a 5 wt % anion-conducting binder solution (3333.4 mg), EtOH (40.4 mg), and ultrapure Milli-Q water (40.4 mg) were used. First, the required amount of catalyst powder was weighed in a glass bottle, followed by the

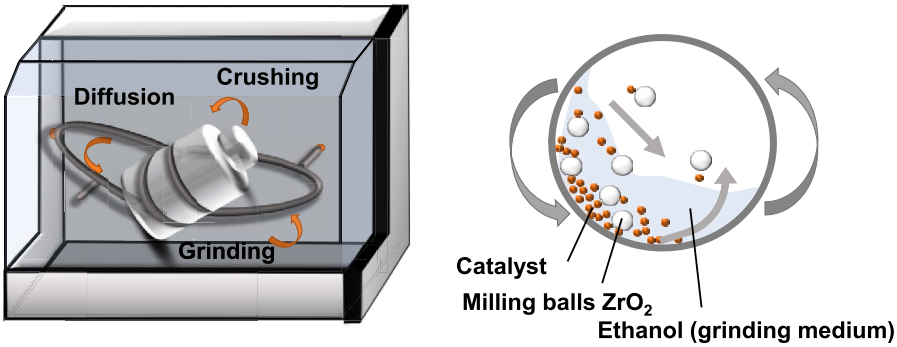

Fig. 1. Illustration of tumbler milling (or mixing): The 3D movement tumbles the powders up and down, while gravity plays the main role in milling (solid and liquid, with or without milling agents).

addition of Milli-Q water. The mixture was dispersed for 5 min with a rotating disperser at 4000 rpm (IKA® Ultra-Turrax®). Next, the binder solution (5 wt%) and EtOH were added to the catalyst dispersion, followed by 5 min Ultra-Turrax® dispersing. 10 min of ultrasonic (US) horn treatment led to final ink homogenization. The catalyst dispersion was continuously cooled inside an ice bath. For Ni_3Fe-LDH-based inks, seven dispersion media (DM) were used (described below). The final dispersion homogenization was set to 10 or 30 min of US horn treatment, while the remaining steps remained unchanged. The total solid content of the catalyst and binder in the catalyst inks was 2 wt%, the binder comprised 20 wt% and 25 wt% of the total solid content for Ni_3Fe-LDH and Pt/C inks, respectively.

For catalyst dispersion optimization, seven DMs were selected: EtOH, EtOH–H_2O 1:1 (meaning the solvents were also mixed in a 1:1 mass ratio), EtOH–H_2O 3:1 (meaning the solvents were also mixed in a 3:1 mass ratio), 2-propanol(i-PrOH)-H_2O 1:1, i-PrOH-H_2O 3:1, and 1-propanol(n-PrOH)-H_2O 1:1, n-PrOH-H_2O 3:1. The DMs were chosen based on multiple factors, including the need for fast evaporation during electrode manufacturing at 80 °C [40], low hazardous solvents commonly being used in fuel cell or electrolyzers production [41], and the previous optimization outcomes [42,43] for Ni–Fe-based catalysts. Further, the selection of DM was guided by solvent properties influencing colloidal stability and ink formation, including the dielectric constant, viscosity. EtOH and n-prop differ in these parameters, with n-prop exhibiting a lower dielectric constant and slightly higher viscosity compared to EtOH (Table S1). These properties can improve particle wetting and reduce particle mobility, thereby suppressing re-agglomeration during dispersion. Therefore, both alcohol-based systems were investigated to evaluate their influence on dispersion stability and electrode performance. As the "baseline" DM, EtOH:H_2O 1:1 was chosen.

2.4. ζ-potential and DLS

Particle size and particle size distribution were analyzed using the dynamic light scattering (DLS) method and ζ-potential determination by electrophoretic light scattering (ELS) using the Litesizer 500 by Anton Paar. The evaluation was performed with the *Kalliope* software. For baseline ζ-potential measurements of Ni_3Fe-LDH powder in ultrapure Milli-Q water, the catalyst was used in a solid concentration of 2 wt% and dispersed over 30 min by means of ultrasonic horn treatment, while continuously being cooled inside an ice bath. The baseline polymeric binder analysis was conducted on a 0.4 wt% binder dispersion (corresponding to the binder concentration in the final catalyst dispersion); dilution was achieved by the addition of ultrapure Milli-Q water. The polymeric binder samples were analyzed immediately after dilution and with an additional 30 min of ultrasonic horn homogenization. For tests without added binders, the catalyst concentration was kept 2 wt% in corresponding solvents. For the ζ-potential analysis of the final catalyst inks, the dispersions were used as prepared without additional dilution (see the catalyst ink preparation section).

For the catalyst cluster size analysis (intensity-weighted hydrodynamic equivalent diameter, D_H further) and size distribution of milled and initial powders, the particles were dispersed in ultrapure Milli-Q water using a vortex mixer for 5 min. For the DLS analysis of catalyst dispersions with or without binders, these were diluted 50 times with the corresponding stock solvent or solvent mixture. The final solid concentration yielded 0.4 wt%. The grade of dilution can affect the final agglomerate size of particles measured by DLS, as has been shown in previous studies (increased dispersion dilution led to decreased carbon agglomerate sizes, although the effect of dilution was less than 20%) [44]. Analysis of diluted catalyst inks could distort the description of the real dispersion as the former decreases the agglomeration kinetics [45]. However, as the dilution was kept identical for each analyzed ink, the obtained values were comparable to each other. For DLS and ζ-potential analysis, the properties of the used mediums are included as externally measured values or values calculated from literature. The refractive index, as well as the dielectric constant of solvents and solvent mixtures used for data evaluation were calculated according to literature [46–51]. The used values for all solvents and solvent mixtures are summarized in Table S1.

2.5. Electrode and membrane electrode assembly fabrication techniques

The electrodes were prepared using an automatic spray coater (Exactacoat by SONO-TEK). First, the pre-cut Ni PTLs were fixed on the 80 °C heated vacuum plate and held by a stainless-steel frame, which prevented the PTLs from making occasional moves. The catalyst ink was directly deposited onto the PTLs in a meandering pattern. To ensure a high level of catalyst layer homogeneity, the layers were sprayed in both the x- and y directions with positive and negative offsets of one third of the sprayed line width. The catalyst loading was controlled through the number of sprayed layers. On the anode side, a loading of 5 mg cm^{-2} Ni_3Fe-LDH was used for an electrode morphology comparison and single-cell performance evaluation; the long-term operation tests were conducted on MEAs with 2 mg cm^{-2} loaded anodes. On the cathode side, 0.6 mg_{Pt} cm^{-2} of the catalyst were deposited. The exact catalyst loading was monitored gravimetrically through the weight increase of a reference sample that was coated in parallel with the electrodes. Before single-cell assembly, the membrane and both the anode and cathode were soaked for 3 h in a 1 M KOH electrolyte for pre-conditioning. The MEAs were assembled in a wet state at room temperature.

2.6. Single-cell assembly and electrochemical measurements

All electrochemical tests were conducted using a custom-made cell hardware with an active area of 5 cm^2, and full Ni serpentine flow-fields on both the anode and cathode sides (Fig. S1). MEA compression was ensured by means of polytetrafluoroethylene (PTFE) foils that were used

as sealing, which were 250 μm-thick on the cathode side and 500 μm-thick on the anode one, which compressed the GDEs on both sides. To prevent any electrical contact between the conductive components, reinforced PTFE foils were positioned between the stainless steel end plates and flow-fields. For heating the system, including the cell and electrolyte, heating elements were connected to both flow-fields. The cell temperature was set to 60 °C and controlled by a thermostat through heating sensors connected to the cell. The anode and cathode sides were fed separately with KOH at flow rates of 5 mL min^{-1} cm^{-2}, while membrane pumps were used for electrolyte circulation during the measurement. A level sensor (TURCK GmbH & Co. KG) connected to the water supply system ensured constant electrolyte concentration. Before connecting the single-cells, nitrogen gas was bubbled through the entire test station, including the electrolyte tanks with the electrolyte inside for degassing (for CO_2 displacement) for at least 2 h. For all electrochemical tests, a battery cycler potentiostat workstation (BioLogic Science Instruments, BCS-815, 15 A max., 10 kHz max.) was employed.

The experimental protocol was implemented in accordance with the European Union's standardized measurement procedures for low-temperature water electrolysis [52]. The break-in procedure started with a 3 h open circuit potential (OCP) step to heat up and equalize the electrolyte between cells and the test station. Then, a linear voltammetry sweep (LSV) was performed with a scan rate of 5 mV s^{-1} between 1.4 and 2.1 V, followed by a conditioning step at a constant current of 1 A cm^{-2} for 4 h. The linear sweep ensured the cell's functionality, whereas the constant current step activated the catalysts. Furthermore, the actual single-cell testing started with a polarization curve recorded in galvanostatic mode. Current densities from 0.016 A cm^{-2} up to 2 A cm^{-2} were held for 1 min each (with a step of 0.016 A cm^{-2} from 0.016 to 0.12 A cm^{-2}, a step of 0.02 A cm^{-2} from 0.12 to 0.2 A cm^{-2}, 0.05 A cm^{-2} between 0.2 and 1.4 A cm^{-2}, and 0.1 A cm^{-2} up to 3 A cm^{-2}). The voltage limit was set to 2.1 V. Two consecutive polarization curves were recorded. The second was selected for evaluation and the full conditioning of the cell was confirmed by comparing the two U–I curves. Next, galvanostatic electrochemical impedance spectroscopy (GEIS) measurements were taken at 20 points, with current densities ranging from 40 mA cm^{-2} to 2 A cm^{-2}, an amplitude of 10% direct current (DC), and a frequency from 0.1 Hz to 10 kHz. The corresponding current densities were held for 5 min each before the GEIS analysis. The high-frequency resistances (HFRs) were used for further iR-correction of the polarization curve. This protocol (break-in step, U–I curve, GEIS measurements) constituted a short-term single-cell performance test of 15 h. To perform the 1000 h long-term operation test, loops were included in the measurement protocol. After each technique combination of a polarization curve and GEIS measurements, 1 A cm^{-2} were held for 100 h. For the evaluation of impedance spectra, the software BT-lab V 1.55 and the tool *Zfit* were used. The equivalent circuit for data fitting consisted of two R-CPE parallel combinations in series with a resistor, as used in previous studies (Fig. S2) [41,53–55]. The voltage efficiency η_{HHV} was calculated using equations S1.1-S1.3. E° was set to 1.199 V, the theoretical thermodynamic voltage of water electrolysis at 60 °C.

The electrode's internal resistance, which contains interfacial contact and bulk resistances, was tested in a full single-cell set-up, where the anode electrode was sandwiched between two copper plates (Fig. S3). Instead of a membrane, a PTFE foil with the same thickness (60 μm) was used, and instead of the cathode a nickel foam with the same thickness as carbon paper (370 μm) was used. The cables (two voltage and two current cables) were connected to the copper plates, each pair (voltage–current cable) was placed on one copper plate. 15 A ($I_{applied}$, 3 A cm^{-2}) were applied to the cell and the overall voltage was measured after 5 min of voltage value stabilization. The electrode contact resistance was calculated as follows:

$$\frac{E_{cell\,measured}}{I_{applied}} = R_{measured} \tag{1.1}$$

$$\left[R_{measured}\ (m\Omega) - R_{2x\ copper\ plates}(m\Omega)\right] * A_{cell} = R_{electrode} \tag{1.2}$$

$R_{2x\ copper\ plates}$ (internal resistance of the copper plates) was measured by applying current to only one copper plate and then multiplied by 2. A_{cell} is the active cell area (5 cm^2) and $R_{electrode}$ is the final electrode internal specific resistance.

2.7. Physical characterization

The catalyst structure was confirmed by X-ray diffraction (XRD) using a D8 Discovery X-ray Diffractometer with Cu-K_α radiation (0.154 nm) in Bragg–Brentano geometry with a 2θ range from 5° to 70°.

To confirm a stable LDH structure, transmission electron microscopy (TEM) images were obtained using a FEI Titan, 80–300 TEM with a cesium corrector for the objective lens (CEOS GmbH) [56]. The microscope was operated at 300 kV. Scanning Electron Microscopy (SEM, Gemini Ultra Plus 500, Zeiss) confirmed the decreased catalyst agglomerate size in powder and revealed the altered catalyst layer structure.

Energy-dispersive X-ray analysis (EDX) was performed using the Zeiss Gemini Ultra Plus device at 20 kV operation voltage for the elemental composition study.

Raman spectroscopy was operated using the WITec alpha300 R confocal Raman device at a laser wavelength of 532 nm and a power of 1 mW. The aperture was fixed at 50 × 1000 μm, and the spectral resolution was ≈1 cm^{-1}. A single spectrum was accumulated at an integration time of 3 s, with the obtained signals averaged over several single scans.

X-ray photoemission spectroscopy (XPS) spectra were collected with a Phi5000 VersaProbe II from ULVAC-Phi Inc with Al K_α serving as the monochromatic source (1.486 keV). The powder samples were pressed onto an indium foil fixed with clamps on a sample holder. The survay spectra were obtained at 187.5 eV pass energy, at 0.8 eV per step, and 100 ms per step. The detailed core-level spectra were recorded with a pass energy of 23.5 eV and 0.1 eV per step. Charge-correction was conducted by setting the peak of C–C 1s to 285 eV. For the fitting, Shirley background was used.

The geometric surface area was obtained by means of N_2 adsorption analysis according to the Brunauer-Emmet-Teller (BET) method with a Gemini VII (Micromeritics) device. Prior to the analysis, the samples were outgassed for at least 24 h at 80 °C under a vacuum.

3. Results and discussion

3.1. Characterization of the catalyst powders

This section aims to analyze the impact of the catalyst milling process on the Ni_3Fe-LDH powder. First, the changes or stagnation of the catalyst are explored at the nanoscale by TEM, followed by an investigation of the particle cluster size in terms of their geometric surface area and hydrodynamic diameter (D_H).

To confirm the preservation of the LDH structure for the milled catalyst, a TEM analysis was conducted. Fig. 2a shows the structures of the initial and milled Ni_3Fe-LDH powders. The TEM images approve the existence of the LDH plates, revealing the characteristic stacked nanosheets that are known from the literature [9,57,58]. The corresponding EDX mappings presented in Fig. S4 do not reveal differences either in the Ni to Fe distribution or the elemental atomic ratios. For the initial powder, the analysis revealed 74 at% Ni and 26 at% Fe, whereas for the milled catalyst 76 at% Ni and 24 at% Fe were found, being equal within the accuracy of the EDX. These observations confirm that the milling process did not harm the sheet structure of the catalyst. Fig. 2b (1–4) presents the SEM images of the initial Ni_3Fe-LDH agglomerates (1–2) and the fine catalyst powder resulted after milling (3–4) at x1k and ×100k magnification. Directly after synthesis, the catalyst agglomerate

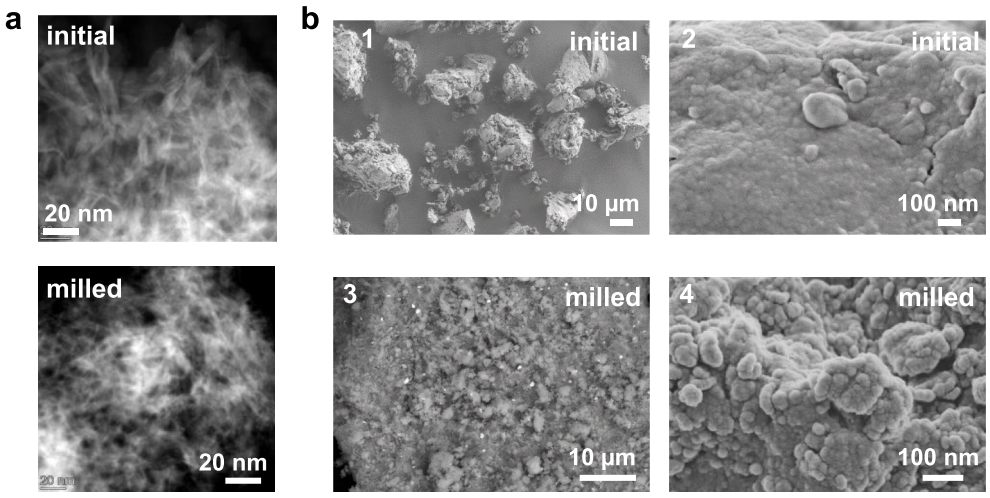

Fig. 2. Changes at the particle level: (a) STEM images of initial and milled Ni_3Fe-LDH catalyst powders; (b) SEM images of initial catalyst agglomerates and milled fine powder at x1k (1 and 3) and x100k (2 and 4) magnifications.

size is non-uniform and exhibits a broad size distribution. Starting from nanometer-scale agglomerates, the particles grow to sizes of 1 µm and even up to 100 µm; an overview at lower magnification is presented in Fig. S5. Based on the experimental observations made in this study, larger particles of the initial catalyst cannot be fragmented and broken down during the catalyst dispersion preparation. After milling, the resulting fine powder is predominantly loose (Figs. 2b and 3), and the resulting catalyst clusters have a size of 100–300 nm with minor units of 30 nm (Figs. 2b and 4).

To evaluate the geometric surface area of both catalyst powder types, a BET analysis was performed. To ensure the measurement's reproducibility, three batches of each catalyst type were analyzed. As is shown in Fig. 3a, the catalyst milling significantly increased the geometric surface area of Ni_3Fe-LDH from (8.51 ± 0.01) m^2g^{-1} to (75.03 ± 0.09) m^2g^{-1}. The 8.8-fold increase is qualitatively consistent, as the agglomerate size becomes smaller due to the milling process. The higher BET value reflects a larger physical particle surface area, which is relevant for catalyst ink processing and CL formation rather than a direct measure of electrochemically active area. In MEA fabrication, reduced agglomeration can improve dispersion quality and suppress sedimentation, supporting a more homogeneous catalyst and binder distribution. This, in turn, increases the likelihood of continuous ionic and electronic transport pathways and more uniformly distributed TPB regions, providing a plausible basis for improved catalyst layer utilization.

To assess the hydrodynamic diameter (D_H) of each catalyst type, DLS measurements were performed. The size and distribution reproducibility were confirmed by repetition of the DLS measurements, which were conducted on three different catalyst batches for both powder types. These results, including the particle size distributions with filled area error bars, are presented in Fig. S6a–c. The initial powder demonstrated a bimodal particle size distribution, with peaks occurring at approximately D_H of 400 nm and 6000 nm, corresponding to the

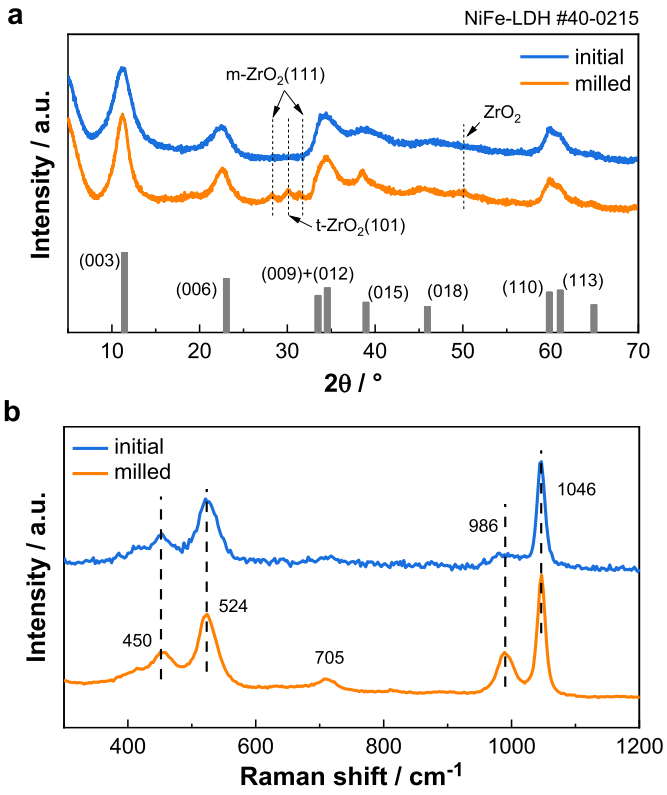

Fig. 4. (a) XRD profiles; and (b) Raman spectra of initial and milled catalyst powders.

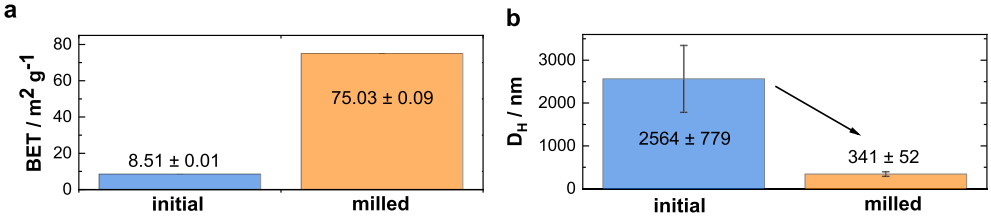

Fig. 3. *(a) BET surface of initial and milled catalyst powders; (b) hydrodynamic diameter (D_H) values of initial and milled catalyst obtained on a catalyst dispersed in ultrapure Milli-Q water.*

smaller and larger and broader D_H distribution peaks, respectively (Fig. S6a). For the milled catalyst, a unimodal D_H size distribution was achieved (Fig. S6b). Thus, the milling process not only shifted the D_H to lower values but also narrowed and changed the size distribution from a bimodal to a unimodal one. Considering both distribution peak values, the averaged D_H for the initial catalyst powder resulted in (2594 ± 779) nm, whereas for the milled powder (341 ± 52) nm were calculated (Fig. 3b). Consequently, a 7.5-fold decrease in the averaged D_H was obtained. Additionally, the reproducibility among different batches was enhanced, as indicated by the decreased error bar for the milled catalyst.

These experiments were performed to set a baseline for the D_H values of both powder types. The obtained numbers imply the expected value range for further studies (described in the Section "Cluster size analysis"), where a DLS analysis is presented for catalyst dispersions containing additional components as solvents and the anion-conducting binder.

Typically, an increase in a three-dimensional object results in a proportional rise in its surface area. Published experimental data [59,60] suggests that the relationship between size (mean diameter) and specific surface area does not necessary follow this expected trend. Especially for complex structures with aggregation and porosity, the layering of sub-structures or roughness of the relationship between surface area and size might not follow simple geometric rules [61,62]. In this case, both the DLS and BET analyses demonstrated that a decrease in particle size corresponds to an increase in surface area.

The structural characteristics of the initial and milled Ni_3Fe-LDH were investigated via XRD analysis. The XRD profiles are presented in Fig. 4a. As heat can be generated and accumulated during milling due to the friction of catalyst powder and grinding balls, the LDH structure might experience structural changes and even a collapse, as is known from thermal treatment experiments on LDH-based species [36,63,64]. The main characteristic peaks for NiFe-LDH at 2Θ values of ≈12, 23, 35, 60° corresponding to (003), (006), (012), and (110) lattice planes (JCPDS#40-02 15 NiFe-LDH), respectively, were observed for both catalysts [19,20,65]. For the milled catalyst, a minor amount of abrasion leftovers of ZrO_2 was detected at between 27° and 33° peaks for monoclinic m-(111) and tetragonal t-(101) ZrO_2 were found [66]. The low intensity of these reflections indicates trace-level abrasion. ZrO_2 is a wide-band-gap oxide and is generally electronically insulating [67]. Zirconia is further considered an oxide with poor intrinsic electrocatalytic activity towards the OER. Stabilized zirconia is widely used in electrochemical systems primarily for its ionic conductivity at elevated temperatures, typically above 700–800 °C, far beyond the operating conditions of the single-cells investigated in this work [68]. Under the present electrolysis conditions, the ionic conductivity of zirconia is negligible, while its electronic conductivity remains insignificant [69]. Furthermore, zirconia is commonly employed as a chemically stable and inert support material rather than as an active electrocatalyst. For example, enhanced OER performance has been reported for IrO_x supported on ZrO_2, where the catalytic activity originated from the supported Ir phase rather than zirconia itself. These finding were obtained under acidic PEMWE conditions [70], which further differs from alkaline AEMWE environment studied. In alkaline media, zirconia formed on zirconium substrates has shown some OER activity only under conditions not comparable to the AEMWE operating conditions, specifically, at temperatures higher than 375 °C. In this study, the observed activity was associated with interfacial effects and structured oxide layers rather than dispersed ZrO_2 particles themselves [71].

Considering the trace amount of ZrO_2 detected in this work, a beneficial contribution to the observed electrochemical performance is unlikely. Therefore, the overall performance improvement observed for the milled catalyst indicates that the enhanced electrode properties are primarily governed by milling induced dispersion effects, including reduced agglomeration, improved CL homogeneity, and enhanced CL–PTL contact. Based on this discussion, ZrO_2 contamination is considered negligible and is not treated as a relevant factor in further analysis. Nevertheless, further optimization of the milling process is needed to avoid any grinding ball abrasion in the future.

Based on the XRD results observed, no changes in Ni_3Fe-LDH catalyst structure, phase, or crystallinity of the Ni_3Fe-LDH was detected. Considering these results and the observations obtained from TEM images, it can be concluded that the LDH structure did not experience significant changes following the milling treatment.

Raman spectroscopy was performed to complement the results of XRD (Fig. 4b). For the initial Ni_3Fe-LDH catalyst, the characteristic Raman bands at ≈450 cm^{-1} and ≈524 cm^{-1} were detected, which are indicative of Fe^{3+}/Ni^{2+}-*O*-Ni^{2+} and Fe^{3+}-*O*-Fe^{3+} bonds, respectively [16,72]. The minor band at ≈705 cm^{-1} is associated with hydroxyl group Ni^{II}–*O*–H [73], whereas the band at ≈986 cm^{-1} is attributed to the nitrates (NO_3^-), remaining from the educts of the catalyst synthesis, and ≈1046 cm^{-1} to the N–O or C–O stretching modes of the interlayer anions CO_3^{-2}/NO_3^- [74,75]. Ni was found in the oxidation state +2, as expected for the non-oxidized pristine catalyst. The peak intensity ratios for the ≈450 cm^{-1} and the ≈524 cm^{-1} bands is consistent with those reported in the literature [76,77], suggesting that the milling process did not affect the bond lengths. After milling, however, a change in the intensity ratios of the bands at ≈986 cm^{-1} and ≈1046 cm^{-1}, associated with the interlayer structure, was observed, with the former becoming more pronounced. Band intensity in Raman spectroscopy is dependent on parameters such as the molecular polarizability or concentration of the active groups. Here, the milling process seems to have impacted the polarizability of certain bonds, specifically NO_3^-. Given that no structural changes were detected by XRD analysis, this shift in intensity ratio does not imply a significant change in the catalyst's composition. This observation indicates that while the milling process may affect certain aspects of the catalyst's properties, it does not fundamentally alter its chemical structure.

XPS analysis was performed on the initial and milled Ni_3Fe-LDH catalysts to investigate the chemical composition, possible changes in the oxidation states, and electronic structures. Previous studies have suggested that ball milling enhances the binding strength of oxygenated intermediates of Ni–Fe-LDH and to shift the electron-equilibrium states into electron-rich structures [20]. Fig. 5 presents the high-resolution XPS spectra of O 1S (a) and Ni 2p (b) of the initial and milled powders; the survey spectra are shown in Fig. S7a. In contrast to the XRD data, which represents the bulk sample, the XPS data, reflecting a local spot within the catalysts' batch only, indicates a negligible presence of ZrO_2 abrasion. From the survey spectra, no additional elements and contaminations were identified. The O 1s spectra (Fig. 5a) displays a minor M − O oxide compound at 529.3 eV, a hydroxide M − OH (Ni^{2+}-, Fe^{3+}-hydroxide) at 531.3 eV, and adsorbed water at 532.8 eV. The high-resolution spectra of Fe 2p (Fig. S7b) displays the characteristic peaks for Fe^{3+} in Ni_3Fe-LDH at approximately 724.8 eV and 712.4 eV, corresponding to Fe 2p1/2 and Fe 2p3/2, respectively. For both powders, Ni presents the two spin–orbit coupling doublets of Ni 2p1/2 and Ni 2p3/2 (Fig. 5b). Positions and areas of the fitted peaks are presented in Table S2. The high-resolution spectra reveal no obvious differences between the initial and milled catalysts.

Comprehensive analyses using XRD, Raman spectroscopy, and XPS have demonstrated that the milling of catalyst powder does not induce notable intrinsic alterations of the LDH structure, elemental oxidation states, composition, phase, or crystallinity. This may be supported by the presence of EtOH as a milling agent, which limits the mechanical impact that could lead to structural changes [36]. On the other hand, milling positively influenced the size of the catalyst clusters, noticeably reducing them, and increasing the accessible geometrical surface area, as proven by BET analysis, which is integral to the catalyst's efficiency. Consequently, the performance differences discussed later are most plausibly attributed to these extrinsic, processing-relevant changes, namely improved physical accessibility and dispersion behavior, which govern CL formation, CL–PTL interfacial contact, and effective catalyst utilization in the MEA, rather than to a fundamentally altered active

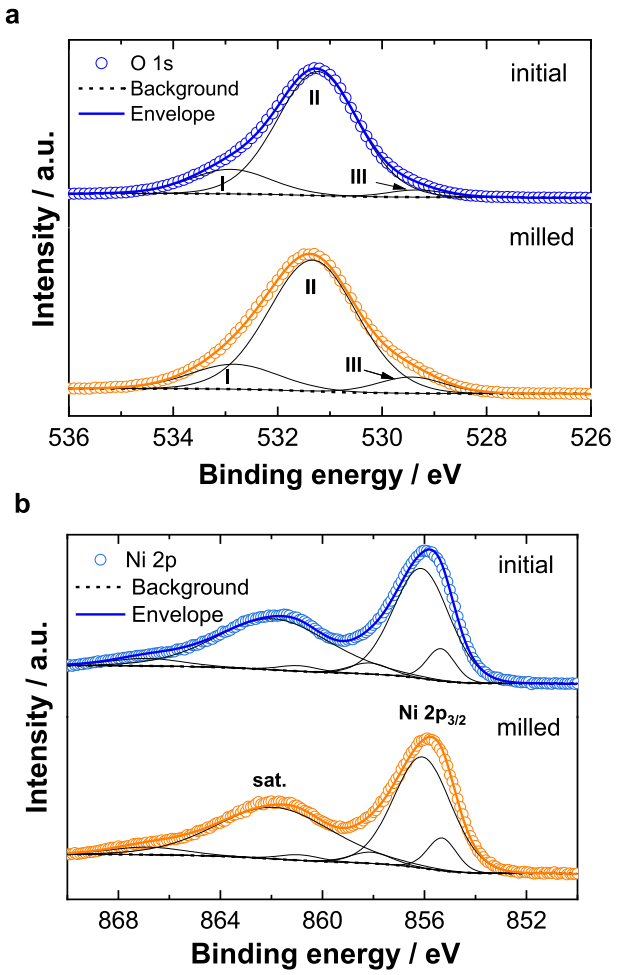

Fig. 5. High-resolution XPS spectra of: (a) O 1s and (b) Ni 2p of the initial (blue) and milled (orange) catalyst powders. The deconvoluted peaks for the O 1S spectra correspond to I: O–O and chemisorbed H_2O (532.8 eV), II: M − OH (531.4 eV), III: M − O, lattice oxygen (529.3 eV); the Ni $2p_{3/2}$ and satellite peaks were deconvoluted into six peaks. (For interpretation of the references to color in this figure legend, the reader is referred to the Web version of this article.)

phase.

3.2. Catalyst dispersion control

Furthermore, catalyst dispersions based on initial or milled Ni_3Fe-LDH and different dispersion media (DM) were characterized. The study aimed to identify an optimized ink composition that enhances stability and homogeneity compared to the commonly used EtOH:H_2O 1:1 dispersion. For clarity, the EtOH:H_2O 1:1 mixture is further named the "baseline DM" or "baseline dispersion," when the catalyst is added. To set a starting point for subsequent tests, the electronic charge and component stability of the catalyst and polymeric binder, slightly dispersed in ultrapure Milli-Q water, were examined. The interaction of the catalyst with various DMs was explored, stability tests were performed, and the influence of an added binder was analyzed. The inks were examined by both ELS (ζ-potential) and DLS analysis (D_H). Finally, the cluster size reproducibility and size distribution between the baseline dispersion and optimized one were evaluated.

The comprehensive description of dispersions, especially those with complex structures like LDHs and added anion-conducting binders, typically requires the analysis of solid materials' concentration, pH values, size, shape, and the spatial arrangement of components [43,78], as well as agglomeration and ζ-potential consideration. However, this study does not include such an analysis due to incomplete knowledge of the preliminary binder's structure and properties. The morphological behavior (clustering, micelle formation) of the polymer as a function of the used solvents or those concentrations (water volume fraction in dispersion), as is known for Nafion [79–81], is not considered in this work. Instead, we carefully investigate the definition of the polymer ζ-potential, taking the electrophoretic polymer chain mobility into account and maintaining the dispersion pH-values of 6.7 ± 0.2. The dispersion control effort in this section is an additional means of enhancing and facilitating dispersion stability and CL fabrication.

Fig. 6a shows the ζ-potentials of bare catalyst particles, initial and milled, and the diluted anion-conducting binder (0.4 wt%), as-dissolved and after 30 min of US horn treatment; all samples were dissolved in ultrapure Milli-Q water. The four analyzed dispersions were prepared in accordance with the Experimental section. In general, values above 30 mV are considered to enable sufficient repulsion of the agglomerates [82] in order to achieve a stable dispersion [83]. The higher the ζ-potential value, the more stable the dispersion is. The ζ-potentials of (35 ± 1) mV for the initial catalyst and (43 ± 1) mV for the milled catalyst indicate a positive charge of the catalyst clusters. The milled catalyst delivered a higher stability in ultrapure Milli-Q water over a retention time of at least 30 min. The polymeric binder presented a positive ζ-potential of (27 ± 2) mV after being slightly dispersed while decreasing to (24 ± 2 mV) after 30 min. Following the ultrasonic treatment, an elevated stability of the binder dispersion was achieved as indicated by the increased ζ-potential of (47 ± 1) mV. The latter parameter holds greater significance, as it reflects the factual condition and concentration of the binder in the resulting electrocatalyst dispersion. The positive ζ-potential values of the anion-conducting binder meet the expectations, as the binder used contains positively charged cationic moieties. Values of 23 to 27 mV and even around 47 mV highlight a relatively high local charge density along the polymer chains [79], especially for a low-concentration binder dispersion of 0.4 wt%. For comparison, Nafion dispersions typically present ζ-potential values close to 30 mV (absolute value) at concentrations not lower than 8 wt% solids [79]. The ζ-potentials obtained for each species remained stable for at least 30 min, confirming the accuracy of the initial measurements.

Furthermore, the stability of the as-prepared catalyst dispersions, determined by varied DMs and US dispersing times of 10 or 30 min, was assessed (Fig. 6b). These dispersions contained no binder. The varying lengths of the bars show that all factors—catalyst type, DM, and dispersing time—impact ink stability. The dispersions based on the milled catalysts consistently show a higher ζ-potential value. As a rule, the longer dispersing time of 30 min leads to higher ink stability than after 10 min, although the enhancement is smaller in comparison to a changed DM. Interestingly, the inks based on i-PrOH and EtOH lead to less stable dispersions. The most stable catalyst ink, with a ζ-potential value of (70 ± 3) mV, was observed for the milled Ni_3Fe-LDH in n-PrOH:H_2O 1:1 after 30 min of dispersing. In comparison, the baseline dispersion (EtOH:H_2O 1:1) delivered a value of (48 ± 1) mV. This could be attributed to the larger size of the n-PrOH molecule, which can form a larger double layer around the particles than the smaller EtOH molecule. Furthermore, compared to EtOH, n-PrOH exhibits a slightly lower dielectric constant and higher viscosity (Table S1), which can strengthen electrosteric stabilization, reduce re-agglomeration during dispersion, and provide a slower drying window that promotes a more homogeneous final layer formation. This interpretation is consistent with prior ink studies showing that solvent dielectric constant and particle ζ-potential are primary determinants of ink stability, and that higher viscosity can support slow drying and homogeneous film formation [42,44,84]. For subsequent analysis, the focus is placed on the most stable dispersion (n-PrOH:H_2O 1:1), hereinafter termed the "optimized" DM or dispersion, and the baseline dispersion is used as a comparative standard. The ζ-potential values for all other inks are summarized in Table S3.

To investigate the influence of the binder on the stability of the

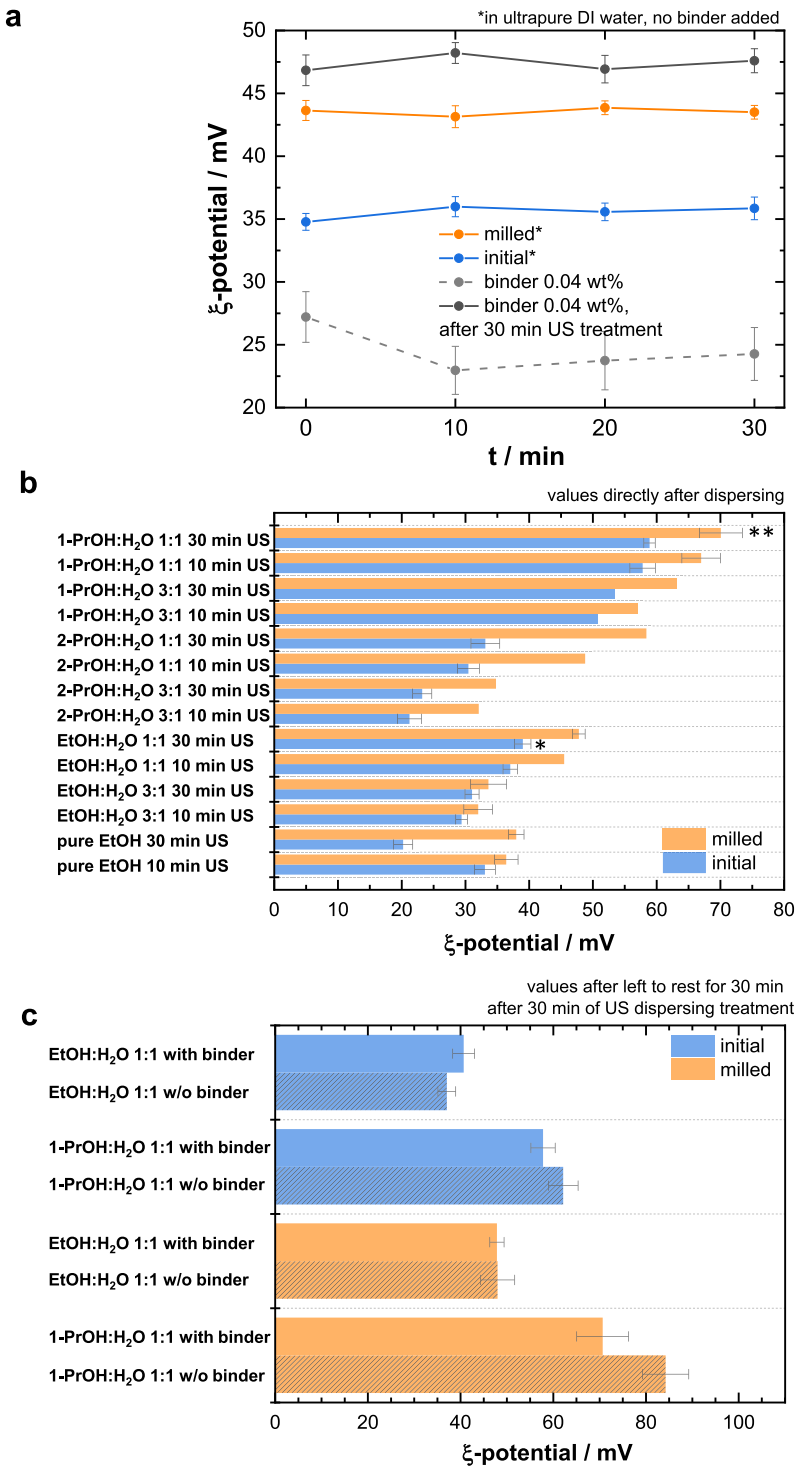

Fig. 6. Dispersion control of an initial (blue) and milled (orange) Ni_3Fe-LDH catalyst: (a) ζ-potential values of the catalyst in ultrapure Milli-Q water after 30 min of US dispersing treatment and within 30 min of rest afterwards, with records of every 10 min, and of the binder dispersion after the solid binder was initially prepared (dissolved) and after 30 min of US dispersing treatment; (b) ζ-potential values of dispersions with varied DMs and dispersing time (10 or 30 min) without the addition of the binder; "*" marks the baseline DM, "**"marks the optimized DM; (c) ζ-potential values of different catalyst inks with (dashed graphs) and without added binders, left to rest for 30 min after a 30 min US dispersing treatment. (For interpretation of the references to color in this figure legend, the reader is referred to the Web version of this article.)

selected catalyst dispersions, further ζ-potential measurements were performed. Fig. 6c displays the ζ-potential values of both the initial and milled catalysts in the baseline and optimized DM, with and without the binder. These values were measured 30 min after dispersion to assess the stability of the eight inks. More detailed data on this is provided in the Supporting Information Fig S8a illustrates the stability of the ink without the binder over 30 min after dispersion, while Fig. S8b shows the stable ζ-potential values of the final dispersions with a binder over 120 min, demonstrating sufficient stability for electrode fabrication. Typically, the addition of a binder to the ink is expected to increase the stability of the dispersion by providing an additional repulsive force amongst the particles in the shape of steric hindrance. Notably, with the binder added, the ζ-potential of the catalyst ink unexpectedly decreased (Fig. 6c colored vs. dashed bars). In general, the decrease of the ζ-potential (in absolute values) reveals weaker electrostatic interactions [85]. Such an effect is often associated with the absence of complete polymeric binder adsorption among the catalyst particles [79,86,87]. Another possible reason for this could be the formation of polymer bridges between the chains, which were indeed adsorbed by the particles [88].

For the DLS tests, all investigated inks were diluted 50-fold (up to 0.4 wt% solid concentration), as the DLS study of diluted inks allows a more accurate particle size analysis [44]. The DLS were performed to evaluate the reproducibility of the formed particle cluster sizes and their distribution within the chosen dispersions.

Earlier, a DLS analysis was conducted on the bare catalyst particles to establish a reference point for the expected cluster size and distribution of sizes (Fig. 3a; Fig. S6). For the anion-conducting binder, preliminary experiments have shown that pure binder dispersion cannot be reliably detected using DLS, even at varying solid concentrations. This may be due to changes in the polymer state, such as dynamic molecular movements. Consequently, it is expected that the measured D_H values for the ink samples only reflect the catalyst particles.

First, the D_H was measured for all chosen catalyst dispersions, revealing consistently lower values for milled catalyst-based inks compared to the initial catalyst-based inks (Fig. S9). As the D_H (and double-layer size) of the particles are affected by the DM used, differences in the values obtained here (Fig. S9) to those measured in pure water (Fig. 3b) are reasonable. The D_H values for inks based on the initial catalyst exhibit significant variability, especially in EtOH-based DMs. There is some correlation with the ζ-potential values, where larger particles, causing sedimentation and agglomeration within the dispersion, result in low stability for pure EtOH and EtOH:H_2O 3:1 inks. To focus on the reproducibility of the catalyst cluster sizes and size distribution of the optimized dispersion compared to the baseline ink, three DLS measurements were conducted on each of these inks (Fig. 7). For dispersions based on the initial catalyst, a partial bimodal distribution with additional peaks at higher sizes, indicating agglomeration, was observed. The milled catalyst-based inks exhibit a unimodal distribution, with a strong size distribution reproducibility for the optimized ink (Fig. 7b). The cluster sizes of the initial catalyst of approximately 670 nm for the baseline ink and 610 nm for the optimized DM were reduced to 402 nm and 333 nm for the milled catalysts in the corresponding solutions, respectively. Because the particle-size distributions are reported as probability density functions, we quantify differences using an uncertainty-aware empirical distance analysis. The full procedure, uncertainty calculation, and the regions exceeding $z > 2$ are provided in the Supporting Information (Fig. S10 and additional explanation to the measurement uncertainty calculation).

Based on the reduced catalyst agglomerate size and enhanced ink stability, the use of milled Ni_3Fe-LDH dispersed in n-PrOH:H_2O 1:1 using ultrasonic horn treatment for 30 min was identified as favorable. The improved CL morphology and electrochemical performance resulting from this dispersion are presented and discussed in the following sections. In addition, the fabrication process itself benefited from the improved dispersion quality, as the absence of large agglomerates reduced clogging of the spray-coating system and enabled more stable, reproducible deposition. This resulted in simplified and accelerated electrode fabrication due to the consistent quality of the dispersions.

3.3. Morphology of the electrodes

Tailoring the morphology of the electrode plays a crucial role in regulating the accessible active sites and catalyst utilization. Not only are the mass transport phenomena controlled by the available active area but also the overall MEA performance due to electrode activity and stability. Excluding any modifications made to the intrinsic structure of the Ni_3Fe-LDH catalyst, a decrease in particle size is also expected to yield a beneficial impact on the electrode utilization.

To investigate the effect of catalyst milling and the enhanced dispersion with increased stability on the resulting catalyst layer, two electrodes with a catalyst loading of 5 mg cm^{-2} were prepared by means of ultrasonic spay deposition. The first electrode, referred to as the initial electrode (or, later, initial MEA), contained the initial catalyst and was prepared with the baseline dispersion. The second electrode, referred to as the milled electrode (or, later, the milled MEA), contained the milled catalyst and the optimized dispersion. The inks included the binder, and the electrodes were prepared in accordance with the experimental section. The top-down view and cross-sectional SEM images of the electrodes are presented in Fig. 8. Both electrodes were fabricated using the catalyst-coated substrate method, creating a porous and structured CL instead of the thin, closed layer as utilized for catalyst-coated

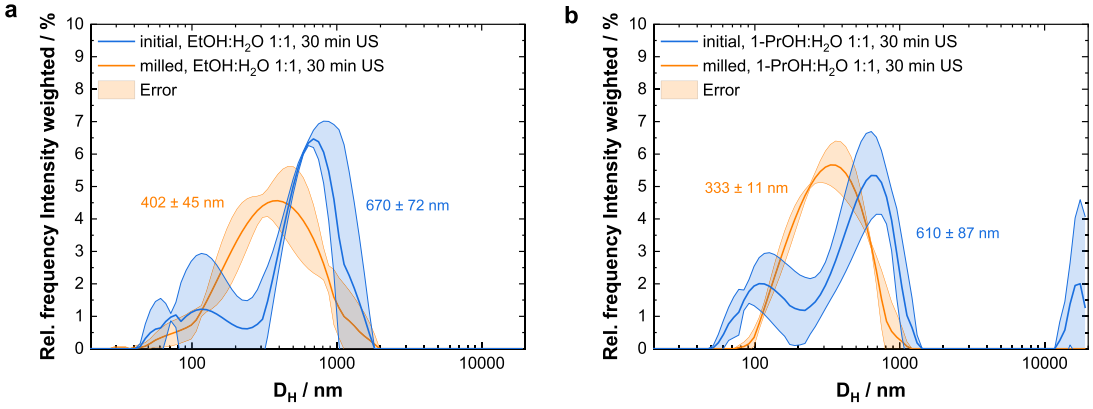

Fig. 7. Catalyst cluster size distribution for initial (blue) and milled (orange) catalyst dispersions, with binder, after 30 min of dispersing US treatment: (a) in baseline (EtOH:H_2O 1:1); and (b) in optimized (n-PrOH:H_2O 1:1) DM. (For interpretation of the references to color in this figure legend, the reader is referred to the Web version of this article.)

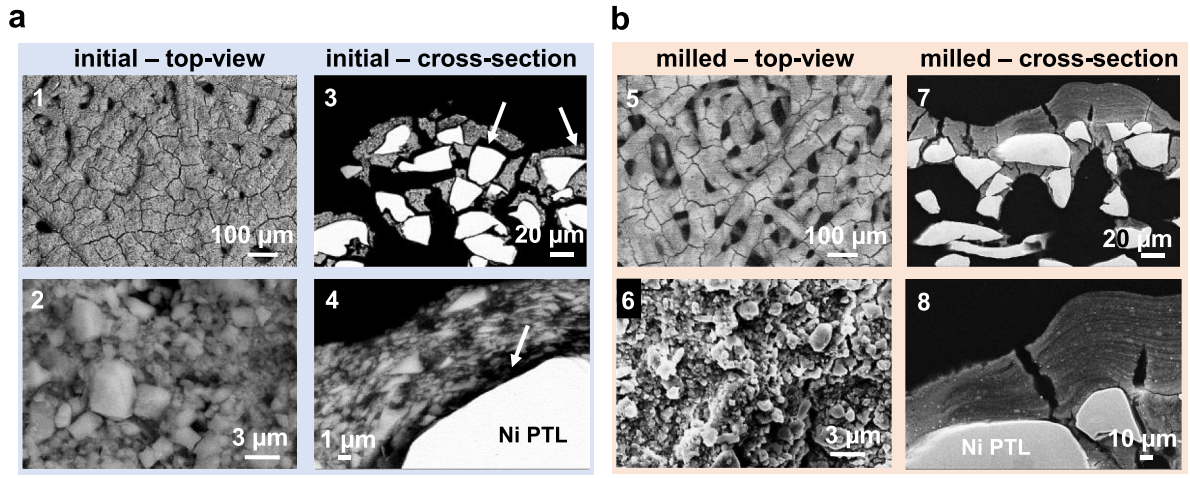

Fig. 8. SEM images at different magnifications of the electrodes from a top-down view or on a cross-section with: (a) initial; and (b) milled catalysts (5 mg cm^{-2} catalyst loading). Arrows indicate delamination of the catalyst layer from the PTL.

membranes. Specifically, the catalyst dispersion covered the fibers of the top few layers of the Ni-PTL substrate. The catalyst layer of the initial electrode shown in image 1 of Fig. 8a does not significantly differ from that of the milled electrode (Fig. 8b, image 5); the slight variation in coverage is attributed to local differences. In both cases, the substrate fibers are well-covered, and some cracks were observed. Typically, strongly pronounced cracks could negatively affect single-cell performance [40,89,90] due to possible catalyst loss and layer delamination, while facilitating faster oxygen bubble detachment in comparison to a closed surface [91]. Nevertheless, in the case of the Ni_3Fe-LDH anode, as proven previously [9,92], and later in this work, these cracks of a few nanometers did not result in poor electrode performance or a lack of durability.

The zoomed-in images of the electrodes (Fig. 8a and b, images 2 and 6) reveal the differences in the CL surface. The catalyst clusters on the milled-electrode present smaller sizes, creating a surface with higher observed roughness. The cross-sectional images expose the strongest difference in the two formed CLs (Fig. 8a and b, images 3 and 4 vs. 7 and 8). The optimized dispersion and use of n-PrOH instead of EtOH appears to increase the adhesion of the CL to the Ni-PTL. The initial electrode exhibits delamination of the CL at some spots (indicated by the white arrows), whereas the optimized milled-electrode CL is fully bonded to the PTL. No significant difference in terms of crack formation is exhibited here, with both electrodes presenting comparable vertical tears in the CL, reaching from the electrode surface to the PTL fibers. The magnified cross-sectional images (Fig. 8a and b, images 4 vs. 8) yet again prove the enhanced distribution of catalyst particles within the milled-electrode. Since catalyst loading and ink composition were kept constant, significant differences in overall catalyst layer thickness are not expected. Cross sectional SEM observations indicate comparable layer thicknesses of approximately 10–30 µm for both electrodes, depending on the analyzed location and local ink distribution within or on top of the PTL fibers. EDX mapping images of electrode cross-sections (Fig. S11) emphasize the differences in elemental distribution homogeneity of the initial electrode and the milled one. Not only can particle size and distribution inhomogeneity be observed but the formation of multiple separated layers within one CL with varying particle density is also apparent (Fig. S11a, image 1, indicated by the white arrow). This phenomenon results from catalyst particle sedimentation in the dispersion during the electrode fabrication process. The smaller particle size and rough topology on the enhanced surface of the milled electrode (Fig. 8b, image 6), as well as the enhanced binder–catalyst distribution observed in the cross-section of image 8 (Fig. 8b) are expected to increase effective catalyst utilization in the MEA by improving ionic and electronic pathway continuity and by reducing local current constriction within the CL. In addition, improved adhesion to the PTL can lower interfacial contact losses.

Taken together, these results establish a clear structure–property link for the improved electrode behavior. The more homogeneous catalyst distribution and reduced sedimentation-driven layering promote a more continuous catalyst–binder network, which supports uninterrupted ionic and electronic transport within the CL. In parallel, the improved CL–PTL contact reduces interfacial voids that can interrupt current pathways. These structural features provide a mechanistic basis for the lower charge-transfer resistance and reduced internal electronic resistance observed later.

3.4. *Performance of the electrodes*

Two MEAs, namely the initial MEA and milled one, were identically fabricated to compare the electrocatalytic single-cell performance of the chosen electrodes. Both MEAs were tested with a catalyst loading of 5 mg cm^{-2} on the anode side. Their polarization curves are presented in Fig. 9a. The milled-MEA showed better performance, reaching 1.83 V at 2 A cm^{-2}, which is 140 mV lower than the initial-MEA, which required 1.97 V at 2 A cm^{-2}. Additionally, as the use of the milled catalyst enhanced dispersion stability, a higher reproducibility of the single-cell performance was achieved, as indicated by the smaller error bars.

To investigate other factors contributing to the enhanced single-cell performance, galvanostatic EIS measurements were carried out. These tests were conducted across the complete range of the current densities examined (0 to 2 A cm^{-2}). The detailed description and results are presented in the Supporting Information (Fig. S12). The HFR-corrected polarization curves shown in Fig. 9a indicate that the performance difference is not due to the Ohmic contribution but mostly the enhanced new electrode structure. While high-frequency intercept is typically attributed to the Ohmic resistance (R_{Ohm}), the semicircle feature represents polarization losses that include a charge-transfer contribution associated with the interfacial OER [52]. Therefore, a lower charge-transfer resistance indicates reduced kinetic and interfacial losses at the catalyst layer at a given operating current, which is commonly interpreted as improved effective catalyst utilization in the MEA [31]. This is also reflected in the analysis of a representative impedance spectrum at 500 mA cm^{-2} in Fig. S13. Both MEAs showed similar R_{Ohm}, whereas the R_{ct} for the milled MEA was significantly lower than that of the initial MEA (113 mΩ cm^2 and 157 mΩ cm^2, respectively), indicating accelerated electrochemical kinetics or improved catalyst utilization [53,93]. Because the Ohmic term remains comparable, the lower R_{ct}

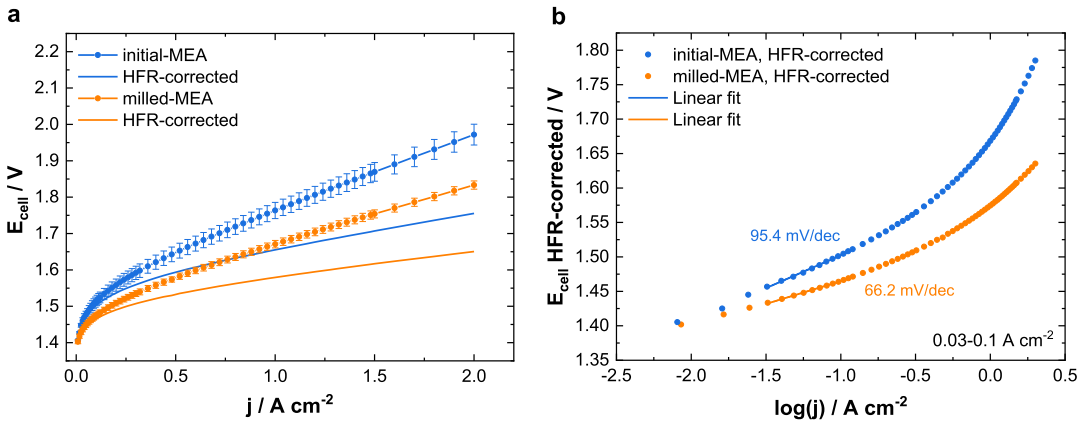

Fig. 9. *(a) Polarization curves of the cell with initial MEA and milled MEA (Ni$_3$Fe-LDH catalyst loading on anodes* 5 mg cm^{-2}), tested at 60 °C and in 1 M KOH electrolyte, including HFR-corrected polarization curves (according to Fig. S12); (b) current density increase rates (E vs log(i)) of the HFR-corrected voltage data from (a), obtained from a linear fit of values between 0.03-0.1 A cm^{-2}.

suggests that the performance enhancement is dominated by reduced polarization losses rather than changes in bulk anion conduction through the membrane or ionomer [31].

As all single-cell components remained unchanged, the observed improvement in performance is likely due to the enhanced anode. The earlier differences in the electrodes' structures observed by SEM (Fig. 8), especially the presence of smaller catalyst clusters and a more homogenous catalyst–binder distribution, combined with the obtained lower R_{ct} values, have a significant influence on the accessibility of catalytically-active sites [20,94]. This interpretation is consistent with literature, showing that improved dispersion and reduced agglomeration in catalyst inks can translate into a more homogeneous CL microstructure, which is accompanied by smaller impedance semicircles and lower apparent charge-transfer resistance [95]. Additionally, the reduced catalyst particle size within the milled-CL can promote a more uniform distribution of gas evolution [4], thereby facilitating the electrode performance. Importantly, this interpretation is consistent with the earlier powder characterization, which showed no evidence for intrinsic catalyst modification by milling. The improved cell performance is therefore not attributed to a chemically different catalyst phase, but to dispersion-driven changes in the CL architecture. Reduced agglomeration and higher ink stability support a more uniform CL formation and improved CL–PTL contact, which lowers interfacial and charge-transfer losses and increases effective catalyst utilization in the MEA.

Fig. 9b shows the cell potential on a logarithmic current scale from the HFR-compensated polarization curves. Linear fits derived over the region of low overpotentials ($\eta = 0.2$–0.45 V) at current densities of 0.03 to 0.1 A cm^{-2} (Fig. S14a) yield the potential increase rates $dE/d\log j$ given in Fig. 9b. For the overpotentials, the Nernst voltage of 1.194 V (60 °C) was considered in accordance with the Nernst equation. The linear fits reached R-squares of 0.998 and 0.997 for the milled MEA and initial MEA, respectively (Fig. S14b). For the single-cell based on the milled MEA, a $dE/d\log j$ slope of (66.2 ± 0.99) mV dec^{-1} was calculated, while the initial MEA delivered (95.4 ± 1.72) mV dec^{-1}. This decreased slope for the optimized milled electrode validates the enhanced single-cell performance and could indicate improvements in the accessibility of catalytically active centers. The lower the $dE/d\log j$ slope is, the faster the charge transfer across the electrocatalytic interface. This hypothesis could suggest increased intrinsic catalytic activity of the milled Ni$_3$Fe-LDH. However, as demonstrated in previous sections, no intrinsic catalyst alterations in bond lengths, oxidation state shifts, or crystallinity modifications were observed. The primary change following catalyst milling and dispersion control is the modified anode CL structure. Consequently, the kinetic improvements can be attributed to enhanced catalyst utilization due to improved catalyst and binder distribution. This in turn indicates enhanced triple-phase boundaries within the CL, as evidenced by the reduced charge–transfer resistance (Fig. S13) [96]. Furthermore, the contribution from the cathode side cannot be fully neglected; however, the separation of the electrode contribution is complex. Nevertheless, the anode is considered to contribute more significantly due to the slower kinetic and higher energy requirements of the OER [97,98].

To evaluate the impact of electrode structural modifications on electrical and interfacial contact properties, the internal [99,100] (interfacial contact and bulk) electrode resistance $R_{electrode}$ was measured in a sandwich-like setup. In this arrangement, as detailed in the Experimental section, the electrode under analysis was placed between two copper plates and integrated into a single-cell configuration. Measuring the interfacial contact resistance of the electrode or PTL is crucial, as it significantly influences electrode or MEA performance [101–103]. Published research, especially in the field of PEMWE, highlights the importance of minimizing interfacial resistance in order to enhance performance and durability.

The R_{Ohm} values obtained earlier are not directly comparable to the resistance values derived from the internal electrode resistance method. The latter specifically tests a single electrode, maintaining direct contact with the copper plates on both the coated and uncoated sides of the electrode. The Ohmic resistance includes, on the other hand, the membrane resistance, as well as that of the electrolyte. Indeed, low interfacial contact resistance can yield decreased Ohmic resistances in a single-cell [104,105].

Fig. 10 presents the internal electronic resistances of the initial and milled electrodes. Values of (26.5 ± 8.8) mΩ cm^2 and (6.7 ± 1.8) mΩ

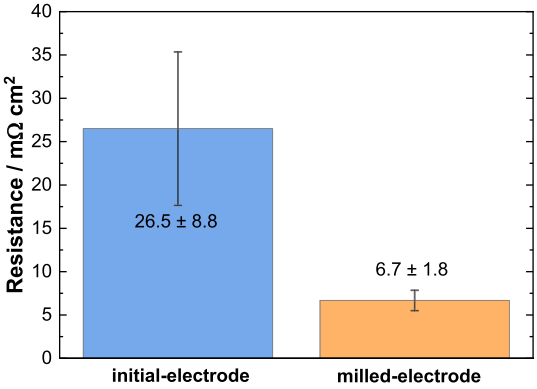

Fig. 10. Internal resistance of the initial electrode and the milled electrode, tested in a single-cell setup.

cm^2 were obtained, respectively, which resulted in a four-fold decrease in the internal resistance of the milled electrode. The smaller error bars further suggest improved reproducibility and reliability. This reduction in resistance directly reflects an increase in internal electronic conductivity, which is due to the finer distribution and smaller size of catalyst particles in the CL, as well as better CL adhesion to the Ni–PTL, an indicator of improved CL architecture. This again confirms that the performance gain is linked to better charge transport through the electrode structure.

The long-term stability of single-cells is a key factor in the commercial use of AEMWEs, ensuring that the optimized electrodes can perform under industrial conditions [94,106,107]. A catalyst loading of 2 mg cm^{-2} on the anode side was chosen to complement and compare the results to the data presented in a previous study [92].

Typically, catalyst loading has a strong impact on the reaction overpotentials [108,109], although in this work, as presented in Fig. S15, the insignificant performance deviations between the cells with catalyst loadings of 2 and 5 mg cm^{-2} on the anode indicate that the higher catalyst loading (or further increase in it) does not offer any performance improvements. With any loading, the milled electrodes outperformed the initial electrodes. Based on these observations, the lower catalyst loading was used for further experiments.

Fig. 11a presents the steady-state durability of the single-cells over 1000 h at 1 A cm^{-2}. Polarization curves were recorded every 100 h of operation, providing insights into the time-dependent cell voltage trend (Fig. S16). For the initial MEA, the best performance was observed after 200 h. This conditioning time is required for several processes: the anode catalyst transforms into an oxidized active state, ion exchange, and full swelling of the binder and membrane, and a critical amount of Fe must be formed within the CL, all contributing to increased catalytic activity [18,92]. The milled MEA reached its highest performance faster, after just 96 h of operation, as is shown in Fig. 11a, and is also proven by the polarization curves and corresponding Nyquist plots (Figs. S16 and S17). As the catalyst cluster size for the initial electrode is inhomogeneous, it is the primary factor contributing to the extended conditioning process. Calculating the degradation rates over the remaining 904 h and 790 h, 62 μV h^{-1} (or 3.66 %) and 84 μV h^{-1} (or 4.68 %) was observed for the milled and initial MEAs, respectively (Fig. S18). In this case, the milled MEA shows a lower degradation rate. Over the full 1000 h of operation, the initial MEA exhibits an overall voltage increase of 45 mV, whereas the optimized MEA exhibits a higher overall voltage rise of 54 mV. Although increased catalyst accessibility in water electrolyzers can boost single-cell performance, faster OER kinetics can also contribute to faster degradation processes [110].

The cell temperature (Fig. 11a, right y-axes, grey) remains tightly controlled around 59–60 °C over the test for both cells, with only insignificant short-term fluctuations (±1 °C) and no pronounced long-term shifts. In principle, a higher operating temperature would be expected to slightly lower the cell voltage at a fixed current density due to improved kinetics and reduced ionic and charge-transfer resistances. However, the magnitude of this effect is typically on the order of 1–2 mV K^{-1}. Therefore, the observed temperature excursions could at most account for only a few millivolts, which is negligible compared to the stronger voltage decrease in the cell conditioning part (<200 h) or the increase in voltage observed over the remaining testing time. Moreover, the steady voltage increase does not track the small temperature variations, supporting that the durability trend is dominated by time-dependent changes in the MEA rather than thermal effects.

The voltage efficiencies, calculated on the basis of equations S1.1–S1.3, underline the performance improvement for the milled MEA, as evidenced by a calculated efficiency of approximately 73%, compared to the initail MEA, which yielded an efficiency of approximately 65% (Fig. 10a).

To further explore the single-cell performance, impedance spectroscopy was employed. In Fig. 11b, the Nyquist plots obtained after the presumed completion of the conditioning period and after 1000 h of operation (end of test, EoT) of both cells are presented. The semicircles of the milled MEA are generally smaller than those of the initial MEA. After 100 h of operation, R_{Ohm} for the milled MEA is 88 mΩ cm^2, whereas for the initial MEA the value was similar, at 90 mΩ cm^2. The main difference is shown by the R_{ct} values of 126 mΩ cm^2 for the milled MEA and 168 mΩ cm^2 for the initial MEA. At EoT, the size of both semicircles increased, resulting in an increase in R_{ct} by 27 mΩ cm^2 and 29 mΩ cm^2 for the milled and initial MEAs, respectively. For both cells, R_{Ohm} changed insignificantly during the observed period, indicating presumed stable behavior in the anion-conducting components and interfacial contacts and conductivity.

To finalize the stability investigation of the chosen electrodes, an SEM characterization was conducted. Fig. 12 presents the SEM images of the initial and milled electrodes from a cross-sectional view at BoT (a) and EoT (b). The images from a top-down view are presented in Fig. S18 and discussed in the Supporting Information, as they display few differences between the initial and milled MEAs. The cross-sectional views of both electrodes reveal some delamination of the CL from the PTL. Both electrodes exhibit a significant morphological reconstruction of the CL, from a finely structured morphology to a sponge-like structure, more precisely aligning with the findings described in our previous work [92]. Interestingly, in contrast to the BoT electrodes, after 1000 h a significant difference between the two anodes was no longer observed.

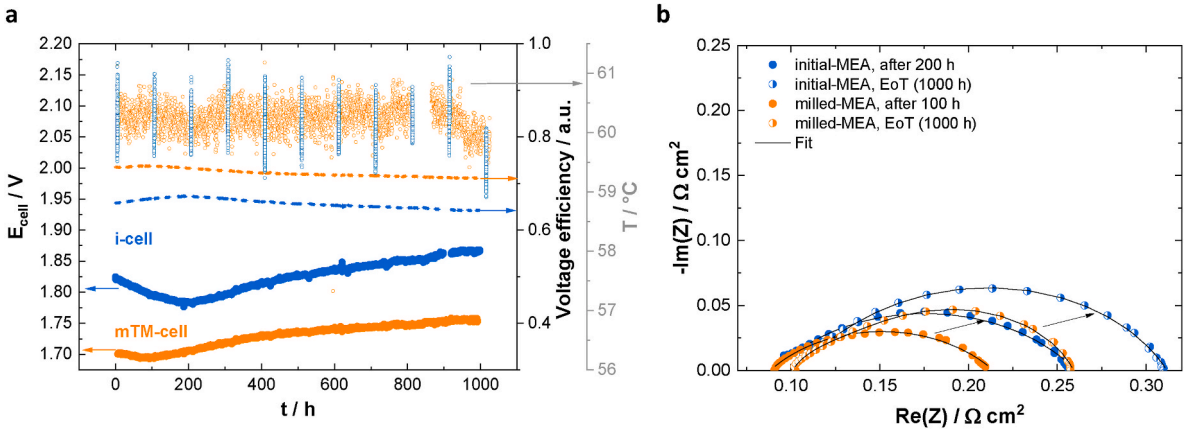

Fig. 11. Stability of the initial and milled MEAs: (a) 1000 h single-cell operation at constant 1 A cm^{-2} in 1 M KOH and at 60 °C, incl. the voltage conversion efficiency plot (dashed graph) and temperature recorded over time (dots graph, grey axis), (b) corresponding Nyquist plots recorded at 500 mA cm^{-2} after break-in (200 h for the initial MEA, 100 h for the milled one) and EoT (1000 h). Anode catalyst loading was 2 mg cm^{-2}.

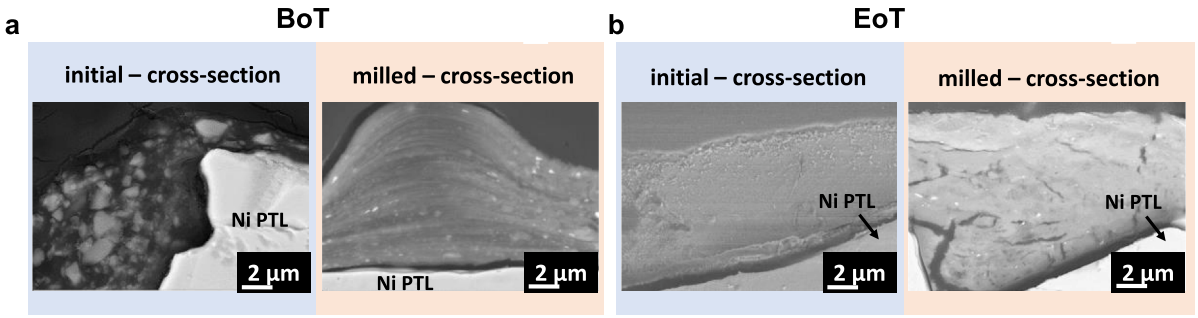

Fig. 12. SEM images at different magnifications of the initial and milled electrodes (2 mg cm^{-2} catalyst loading) from a cross-sectional view of the BoT and EoT (1000 h).

4. Conclusion

In this study, enhancement of the performance of the Ni_3Fe-LDH OER catalyst due to tumbler ball milling was examined. A significant 8.8-fold increase in the geometrical surface area of the catalyst particles was observed after 15 h of milling. At the same time, the particle size distribution transitioned from bimodal to unimodal, with the average hydrodynamic diameter decreasing from 2564 nm to 341 nm. SEM further confirmed the change in catalyst cluster density and dimensions. The LDH structure remained intact after the milling, as was proved by STEM. No modifications in phase, crystallinity, composition, or chemical bond length and oxidation states were observed. By varying several factors in the catalyst ink preparation, including solvents and dispersion durations, an optimized ink for the milled Ni_3Fe-LDH was identified. This optimal formulation consists of a 1:1 mass ratio of n-PrOH to water as the dispersion medium, and ultrasonic horn treatment for 30 min. The catalyst milling and adjustments to the catalyst dispersion resulted in a more homogeneous catalyst layer structure. Consequently, the internal resistance of the electrodes was reduced, and improved catalyst accessibility was achieved, as evidenced by a reduced R_{ct}. This study demonstrates that AEMWE performance is strongly influenced by the electrode structure and the binder–catalyst distribution within the catalyst layer. Achieving optimal catalyst dispersion formulations and high catalyst accessibility is crucial for developing reproducible, high-performance AEMWEs. The reported methodology presents a straightforward, scalable, and effective approach for not only facilitating catalyst ink preparation and enhancing its reproducibility but also for fine-tuning the catalyst layer structure. With the optimized catalyst layer, it was possible to improve single-cell performance by 140 mV, reaching 1.83 V at 2 A cm^{-2} and achieving a durability of 1000 h at 1 A cm^{-2} with a degradation rate of only 3.66%.

CRediT authorship contribution statement

Irina Galkina: Writing – review & editing, Writing – original draft, Visualization, Validation, Resources, Project administration, Methodology, Investigation, Formal analysis, Data curation, Conceptualization. **Alaa Y. Faid:** Resources, Investigation, Conceptualization. **Nikita Grigorev:** Validation, Resources, Investigation. **Wulyu Jiang:** Resources. **Patrick Borowski:** Resources. **Svein Sunde:** Writing – review & editing, Supervision, Resources. **Meital Shviro:** Supervision, Project administration, Investigation, Funding acquisition. **Werner Lehnert:** Supervision. **Fabian Scheepers:** Writing – original draft, Supervision, Methodology, Conceptualization. **Anna K. Mechler:** Writing – original draft, Supervision.

Funding

This work was conducted within the framework of the CHANNEL project. This project received funding from the Fuel Cells and Hydrogen 2 Joint Undertaking (now Clean Hydrogen Partnership) under grant agreement No. 875088. This Joint undertaking receives support from the European Union's Horizon 2020 Research and Innovation program, Hydrogen Europe and Hydrogen Europe Research.

Declaration of competing interest

The authors declare that they have no known competing financial interests or personal relationships that could have appeared to influence the work reported in this paper.

Appendix A. Supplementary data

Supplementary data to this article can be found online at https://doi.org/10.1016/j.ijhydene.2026.155383.

References

[1] Hunter BM, Gray HB, Muller AM. Earth-abundant heterogeneous water oxidation catalysts. Chem Rev 2016;116:14120–36.
[2] Mavrič A, Cui C. Advances and challenges in industrial-scale water oxidation on layered double hydroxides. ACS Appl Energy Mater 2021;4:12032–55.
[3] Chow J, Kopp RJ, Portney PR. Energy resources and global development. Science 2003;302(80):1528–31.
[4] Li D, et al. Durability of anion exchange membrane water electrolyzers. Energy Environ Sci 2021;14:3393–419.
[5] Xu H, et al. Three-dimensional open CoMoOx/CoMoSx/CoSx nanobox electrocatalysts for efficient oxygen evolution reaction. Appl Catal B Environ 2020;265.
[6] Fan K, et al. Nickel-vanadium monolayer double hydroxide for efficient electrochemical water oxidation. Nat Commun 2016;7:1–9.
[7] Xu D, et al. Earth-abundant oxygen electrocatalysts for alkaline anion-exchange-membrane water electrolysis: effects of catalyst conductivity and comparison with performance in three-electrode cells. ACS Catal 2019;9:7–15.
[8] Faid AY, Barnett AO, Seland F, Sunde S. Highly active nickel-based catalyst for hydrogen evolution in anion exchange membrane electrolysis. Catalysts 2018;8:1–8.
[9] Jiang W, et al. Composition-dependent morphology, structure, and catalytical performance of nickel–iron layered double hydroxide as highly-efficient and stable anode catalyst in anion exchange membrane water electrolysis. Adv Funct Mater 2022;32:2203520.
[10] Qiu Z, Tai CW, Niklasson GA, Edvinsson T. Direct observation of active catalyst surface phases and the effect of dynamic self-optimization in NiFe-layered double hydroxides for alkaline water splitting. Energy Environ Sci 2019;12:572–81.
[11] Zhan T, Zhang Y, Liu X, Lu SS, Hou W. NiFe layered double hydroxide/reduced graphene oxide nanohybrid as an efficient bifunctional electrocatalyst for oxygen evolution and reduction reactions. J Power Sources 2016;333:53–60.
[12] Sun Y, Gao S, Lei F, Xie Y. Atomically-thin two-dimensional sheets for understanding active sites in catalysis. Chem Soc Rev 2015;44:623–36.
[13] Lu Z, et al. Three-dimensional NiFe layered double hydroxide film for high-efficiency oxygen evolution reaction. Chem Commun 2014;50:6479–82.
[14] Xiao J, et al. Water-fed hydroxide exchange membrane electrolyzer enabled by a fluoride-incorporated nickel-iron oxyhydroxide oxygen evolution electrode. ACS Catal 2021;11:264–70.
[15] Yu L, Yang JF, Guan BY, Lu Y, Lou XWD. Hierarchical hollow nanoprisms based on ultrathin Ni-Fe layered double hydroxide nanosheets with enhanced electrocatalytic activity towards oxygen evolution. Angew Chemie Int Ed 2018;57:172–6.

[16] Peng L, et al. Atomic cation-vacancy engineering of NiFe-Layered double hydroxides for improved activity and stability towards the oxygen evolution reaction. Angew Chemie Int Ed 2021;60:24612–9.
[17] Dang L, et al. Direct synthesis and anion exchange of Noncarbonate-Intercalated NiFe-Layered double hydroxides and the influence on electrocatalysis. Chem Mater 2018;30:4321–30.
[18] Li Z, et al. Fast electrosynthesis of Fe-containing layered double hydroxide arrays toward highly efficient electrocatalytic oxidation reactions. Chem Sci 2015;6:6624–31.
[19] Song F, Hu X. Exfoliation of layered double hydroxides for enhanced oxygen evolution catalysis. Nat Commun 2014;5:4477.
[20] Zhou D, et al. NiFe hydroxide lattice tensile strain: enhancement of adsorption of oxygenated intermediates for efficient water oxidation catalysis. Angew Chemie Int Ed 2019;58:736–40.
[21] Lu X, Zhao C. Electrodeposition of hierarchically structured three-dimensional nickel-iron electrodes for efficient oxygen evolution at high current densities. Nat Commun 2015;6.
[22] Long X, et al. A strongly coupled graphene and FeNi double hydroxide hybrid as an excellent electrocatalyst for the oxygen evolution reaction. Angew Chemie 2014;126:7714–8.
[23] Liang H, et al. Hydrothermal continuous flow synthesis and exfoliation of NiCo layered double hydroxide nanosheets for enhanced oxygen evolution catalysis. Nano Lett 2015;15:1421–7.
[24] Han N, Zhao F, Li Y. Ultrathin nickel-iron layered double hydroxide nanosheets intercalated with molybdate anions for electrocatalytic water oxidation. J Mater Chem A 2015;3:16348–53.
[25] Lazaridis T, Stühmeier BM, Gasteiger HA, El-Sayed HA. Capabilities and limitations of rotating disk electrodes versus membrane electrode assemblies in the investigation of electrocatalysts. Nat Catal 2022;5:363–73.
[26] Xu Q, et al. Anion exchange membrane water electrolyzer: electrode design, lab-scaled testing system and performance evaluation. EnergyChem 2022;4:100087.
[27] Kreider ME, et al. Understanding the effects of anode catalyst conductivity and loading on catalyst layer utilization and performance for anion exchange membrane water electrolysis. 2024. https://doi.org/10.1021/acscatal.4c02932.
[28] Koch S, et al. The effect of ionomer content in catalyst layers in anion-exchange membrane water electrolyzers prepared with reinforced membranes (Aemion + ™) †. J Mater Chem A 2021;9:15744–54.
[29] Cossar E, Murphy F, Baranova EA. Nickel-based anodes in anion exchange membrane water electrolysis: a review. J Chem Technol Biotechnol 2022;97:1611–24.
[30] Liu SQ, et al. Bi2O3Nanosheets grown on carbon nanofiber with inherent hydrophobicity for high-performance CO2Electroreduction in a wide potential window. ACS Nano 2021;15:17757–68.
[31] Volk EK, Kreider ME, Kwon S, Alia SM. Recent progress in understanding the catalyst layer in anion exchange membrane electrolyzers – durability , utilization , and integration. EES Catal 2024;2:109–37.
[32] Murugaiah DK, Shahgaldi S. Recent progress in understanding the dispersion stability of catalyst ink for proton exchange membrane fuel cell and water electrolyzer. Int J Hydrogen Energy 2024;66:156–69.
[33] Liu C, et al. Fabrication of catalyst layer for proton exchange membrane water electrolyzer: I. Effects of dispersion on particle size distribution and rheological behavior. Int J Hydrogen Energy 2024;52:1143–54.
[34] Cheng X, Fabbri E, Kim B, Nachtegaal M, Schmidt TJ. Effect of ball milling on the electrocatalytic activity of Ba 0.5 Sr 0.5 Co 0.8 Fe 0.2 O 3 towards the oxygen evolution reaction. J Mater Chem A 2017;5:13130–7.
[35] Yagi S, Wada K, Yuuki J, Liu W, Yamada I. Effects of size and crystallinity of CaCu3Fe4O12 on catalytic activity for oxygen evolution reaction. Mater Trans 2020;61:1698–702.
[36] Bhandari S, Schierholz R, Eichel RA, Luna AL, Mechler AK. Exploring the effect of ball milling on the physicochemical properties and oxygen evolution reaction activity of nickel and cobalt oxides. Adv Energy Sustain Res 2024;2400183.
[37] Heo S, et al. Synthesis of Co3O4-Fe2O3 via high-energy ball milling for efficient oxygen evolution reaction in water splitting. J Am Ceram Soc 2025;108.
[38] Stieß M. Mechanische verfahrenstechnik. Springer Berlin; 1994.
[39] Hong S-H, Kim B-K. Effects of lifter bars on the ball motion and aluminum foil milling in tumbler ball mill. Mater Lett 2002;57:275–9.
[40] Zhao J, Li X, Liu Z. The effect of ink dilution and evaporation on the microstructures of catalyst layers in polymer electrolyte membrane fuel cells. Int J Energy Res 2019;43:6799–811.
[41] Faid AY, Barnett AO, Seland F, Sunde S. Tuning Ni–MoO 2 catalyst–ionomer and electrolyte interaction for water electrolyzers with anion exchange membranes. ACS Appl Energy Mater 2021;4:3327–40.
[42] Guo Y, et al. Effect of dispersion solvents and ionomers on the rheology of catalyst inks and catalyst layer structure for proton exchange membrane fuel cells. ACS Appl Mater Interfaces 2021;13:27119–28.
[43] Khandavalli S, et al. Investigation of the microstructure and rheology of iridium oxide catalyst inks for low-temperature polymer electrolyte membrane water electrolyzers. ACS Appl Mater Interfaces 2019;11:45068–79.
[44] Shukla S, Bhattacharjee S, Weber AZ, Secanell M. Experimental and theoretical analysis of ink dispersion stability for polymer electrolyte fuel cell applications. J Electrochem Soc 2017;164:F600–9.
[45] Mewis J, Wagner NJ. Colloidal suspension rheology. Colloid Suspens Rheol 2011:1–393. 9780521515.
[46] Kuchuk VI, Shirokova IY, Golikova EV. Physicochemical properties of water-alcohol mixtures of a homological series of lower aliphatic alcohols. Glas Phys Chem 2012;38:460–5.
[47] Wyman J. The dielectric constant of mixtures of ethyl alcohol and water from -5 to 40. J Am Chem Soc 1931;53:3292.
[48] Bellmann C, Caspari A, Moitzi C, Babick F. Dynamische Un elektrophoretische lichtstreuung. 2018.
[49] Weber MJ. Handbook of optical materials. Boca Raton: CRC Press LLC; 2003.
[50] Da Silva MJ. Impedance sensors for fast multiphase flow measurement and imaging. Elektrotechnik Und Informationstechnik; 2008.
[51] Ritzoulis G, Fidantsi A. Relative permittivities, refractive indices, and densities for the binary mixtures N,N′-dimethylacetamide with methanol, ethanol, 1-butanol, and 2-propanol at 298.15 K. J Chem Eng Data 2000;45:207–9.
[52] Malkow T, Pilenga A, Tsotridis G, De Marco G. EU harmonised polarisation curve test method for Low- temperature water electrolysis. European commission. Joint Research Centre; 2018. https://doi.org/10.2760/179509.
[53] Lettenmeier P, et al. Durable membrane electrode assemblies for proton exchange membrane electrolyzer systems operating at high current densities. Electrochim Acta 2016;210:502–11.
[54] López-Fernández E, et al. Chemistry and electrocatalytic activity of nanostructured nickel electrodes for water electrolysis. ACS Catal 2020;10:6159–70.
[55] Majasan JO, et al. Correlative study of microstructure and performance for porous transport layers in polymer electrolyte membrane water electrolysers by X-ray computed tomography and electrochemical characterization. Int J Hydrogen Energy 2019;44:19519–32.
[56] Thust A, Barthel J, Tillmann KFEI. Titan 80-300 TEM. J large scale Res Facil JLSRF 2016;2:3–6.
[57] Wang Q, et al. NiFe layered double hydroxide nanoparticles on Co,N-Codoped carbon nanoframes as efficient bifunctional catalysts for rechargeable zinc–air batteries. Adv Energy Mater 2017;7:1–7.
[58] He H, et al. Improvement of trisodium citrate-modified nife-layered double hydroxide nanosheets with carbon black for oxygen evolution reaction. Catalysts 2020;10.
[59] Bushell M, et al. Characterization of commercial metal oxide nanomaterials: crystalline phase, particle size and specific surface area. Nanomaterials 2020;10:1–19.
[60] Rahman IA, Vejayakumaran P, Sipaut CS, Ismail J, Chee CK. Size-dependent physicochemical and optical properties of silica nanoparticles. Mater Chem Phys 2009;114:328–32.
[61] Ouf FX, Bourrous S, Vallières C, Yon J, Lintis L. Specific surface area of combustion emitted particles: impact of primary particle diameter and organic content. J Aerosol Sci 2019;137:105436.
[62] Ersahin S, Gunal H, Kutlu T, Yetgin B, Coban S. Estimating specific surface area and cation exchange capacity in soils using fractal dimension of particle-size distribution. Geoderma 2006;136:588–97.
[63] Li L, Feng Y, Li Y, Zhao W, Shi J. Fe3O4 core/layered double hydroxide shell nanocomposite: versatile magnetic matrix for anionic functional materials. Angew Chemie Int Ed 2009;48:5888–92.
[64] Pérez-Ramírez J, Abelló S, Van Der Pers NM. Memory effect of activated Mg-Al hydrotalcite: in situ XRD studies during decomposition and gas-phase reconstruction. Chem Eur J 2007;13:870–8.
[65] Han Y, et al. Preparation of Ni2+- Fe3+ layered double hydroxide material with high crystallinity and well-defined hexagonal shapes. Chem Mater 2008;20:360–3.
[66] Gauna MR, et al. Monoclinic-tetragonal zirconia quantification of commercial nanopowder mixtures by XRD and DTA. Ceram Silikaty 2015;50:318–25.
[67] Emeline A, et al. Spectroscopic and photoluminescence studies of a wide band gap insulating material: powdered and colloidal ZrO 2 sols. Langmuir 1998;14:5011–22.
[68] Badwal S. Zirconia-based solid electrolytes: microstructure, stability and ionic conductivity. Solid State Ionics 1992;52:23–32.
[69] Taubmann J, Sun X, Khajavi P, Jacobsen T, Mogensen MB. A review of the electrochemical properties of stabilised zirconia. Solid State Ionics 2026;439:117165.
[70] Fang SR, et al. Tetragonal ZrO2 supported low-iridium catalyst activating oxygen spillover stabilized lattice oxygen for proton exchange membrane water electrolysis. Energy Environ Sci 2025;18:5470–81.
[71] Matsuzawa K, Ishihara A, Oishi A, Mitsushima S, Ota K. Catalytic activity of zirconia on zirconium for the oxygen evolution reaction in potassium hydroxide. Mater Sci Eng B 2021;267:115112.
[72] Sriram B, et al. Eutectic solvent-mediated synthesis of NiFe-LDH/Sulfur-Doped carbon nitride arrays: investigation of electrocatalytic activity for the dimetridazole sensor in human sustenance. ACS Sustainable Chem Eng 2020;8:17772–82.
[73] Bantignies JL, et al. New insight into the vibrational behavior of nickel hydroxide and oxyhydroxide using inelastic neutron scattering, far/mid-infrared and Raman spectroscopies. J Phys Chem C 2008;112:2193–201.
[74] Diaz-Morales O, Ferrus-Suspedra D, Koper MTM. The importance of nickel oxyhydroxide deprotonation on its activity towards electrochemical water oxidation. Chem Sci 2016;7:2639–45.
[75] Hunter BM, Hieringer W, Winkler JR, Gray HB, Müller AM. Effect of interlayer anions on [NiFe]-LDH nanosheet water oxidation activity. Energy Environ Sci 2016;9:1734–43.
[76] Thangavel P, et al. Graphene-nanoplatelets-supported NiFe-MOF: High-efficiency and ultra-stable oxygen electrodes for sustained alkaline anion exchange membrane water electrolysis. Energy Environ Sci 2020;13:3447–58.

[77] Bai L, Lee S, Hu X. Spectroscopic and electrokinetic evidence for a bifunctional mechanism of the oxygen evolution reaction. Angew Chemie Int Ed 2021;60:3095–103.
[78] Faid AY, Barnett AO, Seland F, Sunde S. Optimized nickel-cobalt and nickel-iron oxide catalysts for the hydrogen evolution reaction in alkaline water electrolysis. J Electrochem Soc 2019;166:F519–33.
[79] Zhang H, Pan J, He X, Pan M. Zeta potential of Nafion molecules in isopropanol-water mixture solvent. J Appl Polym Sci 2008;107:3306–9.
[80] Elliott JA, Hanna S, Elliott AMS, Cooley GE. The swelling behaviour of perfluorinated ionomer membranes in ethanol/water mixtures. Polymer (Guildf) 2001;42:2251–3.
[81] James PJ, et al. Hydration of Nafion studied by AFM and X-ray scattering. J Mater Sci 2000;35:5111–9.
[82] Larsson M, Hill A, Duffy J. Suspension stability: why particle size, zeta potential and rheology are important product technical specialists rheometry products malvern instruments limited. Annu Trans Nord Rheol Soc 2012;20:1999.
[83] ASTM Standard D 4187-82. Zeta potential of colloids in water and waste water, ASTM standard D 4187-82, American Society for testing and Materials,1985. Am Soc Test Mater 1985.
[84] Kukobat R, et al. Essential role of viscosity of SWCNT inks in homogeneous conducting film Formation. Langmuir 2016;32:6909–16.
[85] Lin DQ, Brixius PJ, Hubbuch JJ, Thömmes J, Kula MR. Biomass/adsorbent electrostatic interactions in expanded bed adsorption: a zeta potential study. Biotechnol Bioeng 2003;83:149–57.
[86] Berlinger SA, McCloskey BD, Weber AZ. Inherent acidity of perfluorosulfonic acid ionomer dispersions and implications for ink aggregation. J Phys Chem B 2018;122:7790–6.
[87] Li GF, Yang D, Abel Chuang PY. Defining nafion ionomer roles for enhancing alkaline oxygen evolution electrocatalysis. ACS Catal 2018;8:11688–98.
[88] Ostolska I, Wiśniewska M. Application of the zeta potential measurements to explanation of colloidal Cr2O3stability mechanism in the presence of the ionic polyamino acids. Colloid Polym Sci 2014;292:2453–64.
[89] Kumano N, et al. Controlling cracking formation in fuel cell catalyst layers. J Power Sources 2019;419:219–28.
[90] Tsushima S, Hirai S. An overview of cracks and interfacial voids in membrane electrode assemblies in polymer electrolyte fuel cells. J Therm Sci Technol 2015;10:1–12.
[91] Zeradjanin AR, et al. Rational design of the electrode morphology for oxygen evolution-enhancing the performance for catalytic water oxidation. RSC Adv 2014;4:9579–87.
[92] Galkina I, et al. Stability of Ni–Fe-layered double hydroxide under long-term operation in AEM water electrolysis. Small 2024;2311047:1–14.
[93] Qiu Y, Zhang H, Zhong H, Zhang F. A novel cathode structure with double catalyst layers and low Pt loading for proton exchange membrane fuel cells. Int J Hydrogen Energy 2013;38:5836–44.
[94] Du N, et al. Anion-exchange membrane water electrolyzers. Chem Rev 2022;122:11830–95.
[95] Yang DD, et al. Influence of the dispersion state of ionomer on the dispersion of catalyst ink and the construction of catalyst layer. Int J Hydrogen Energy 2021;46:33300–13.
[96] Breitwieser M, Klingele M, Vierrath S, Zengerle R, Thiele S. Tailoring the membrane-electrode interface in PEM fuel cells: a review and perspective on novel engineering approaches. Adv Energy Mater 2018;8.
[97] Raja Sulaiman RR, Wong WY, Loh KS. Recent developments on transition metal–based electrocatalysts for application in anion exchange membrane water electrolysis. Int J Energy Res 2022;46:2241–76.
[98] Miller HA, et al. Green hydrogen from anion exchange membrane water electrolysis: a review of recent developments in critical materials and operating conditions. Sustain Energy Fuels 2020;4:2114–33.
[99] Phillips R, Edwards A, Rome B, Jones DR, Dunnill CW. Minimising the ohmic resistance of an alkaline electrolysis cell through effective cell design. Int J Hydrogen Energy 2017;42:23986–94.
[100] Ieropoulos I, Winfield J, Greenman J. Effects of flow-rate, inoculum and time on the internal resistance of microbial fuel cells. Bioresour Technol 2010;101:3520–5.
[101] Polonský J, et al. Anodic microporous layer for polymer electrolyte membrane water electrolysers. J Appl Electrochem 2017;47:1137–46.
[102] Lettenmeier P, Kolb S, Burggraf F, Gago AS, Friedrich KA. Towards developing a backing layer for proton exchange membrane electrolyzers. J Power Sources 2016;311:153–8.
[103] Lopata J, et al. Effects of the transport/catalyst layer interface and catalyst loading on mass and charge transport phenomena in polymer electrolyte membrane water electrolysis devices. J Electrochem Soc 2020;167:064507.
[104] Schuler T, et al. Hierarchically structured porous transport layers for polymer electrolyte water electrolysis. Adv Energy Mater 2020;10:1–12.
[105] Lettenmeier P, et al. Comprehensive investigation of novel pore-graded gas diffusion layers for high-performance and cost-effective proton exchange membrane electrolyzers. Energy Environ Sci 2017;10:2521–33.
[106] Pavel CC, et al. Highly efficient platinum group metal free based membrane-electrode assembly for anion exchange membrane water electrolysis. Angew Chemie Int Ed 2014;53:1378–81.
[107] Zeng K, Zhang D. Recent progress in alkaline water electrolysis for hydrogen production and applications. Prog Energy Combust Sci 2010;36:307–26.
[108] Bernt M, Siebel A, Gasteiger HA. Analysis of voltage losses in PEM water electrolyzers with low platinum group metal loadings. J Electrochem Soc 2018;165:F305–14.
[109] Millet P, et al. Electrochemical performances of PEM water electrolysis cells and perspectives. Int J Hydrogen Energy 2011;36:4134–42.
[110] Siracusano S, et al. New insights into the stability of a high performance nanostructured catalyst for sustainable water electrolysis. Nano Energy 2017;40:618–32.